

On the existence, rareness and uniqueness of quenched HI-rich galaxies in the local Universe

XIAO LI,¹ CHENG LI,¹ H. J. MO,² JIANHONG HU,¹ JING WANG,³ AND TING XIAO⁴

¹*Department of Astronomy, Tsinghua University, Beijing 100084, China*

²*Department of Astronomy, University of Massachusetts Amherst, MA 01003, USA*

³*Kavli Institute for Astronomy and Astrophysics, Peking University, Beijing 100871, China*

⁴*School of Physics, Zhejiang University, Hangzhou, Zhejiang 310058, China*

ABSTRACT

Using data from ALFALFA, xGASS, HI-MaNGA and the Sloan Digital Sky Survey (SDSS), we identify a sample of 47 “red but HI-rich”(RR) galaxies with $\text{NUV} - r > 5$ and unusually high HI-to-stellar mass ratios. We compare the optical properties and local environments between the RR galaxies and a control sample of “red and HI-normal”(RN) galaxies that are matched in stellar mass and color. The two samples are similar in the optical properties typical of massive red (quenched) galaxies in the local Universe. The RR sample tends to be associated with slightly lower-density environments and has lower clustering amplitudes and smaller neighbor counts at scales from several hundred kiloparsecs to a few megaparsecs. The results are consistent with the RR galaxies being preferentially located at the center of low-mass halos, with a median halo mass $\sim 10^{12} h^{-1} M_{\odot}$ compared to $\sim 10^{12.5} h^{-1} M_{\odot}$ for the RN sample. This result is confirmed by the SDSS group catalog which reveals a central fraction of 89% for the RR sample, compared to $\sim 60\%$ for the RN sample. If assumed to follow the HI size-mass relation of normal galaxies, the RR galaxies have an average HI-to-optical radius ratio of $R_{\text{HI}}/R_{90} \sim 4$, four times the average ratio for the RN sample. We compare our RR sample with similar samples in previous studies, and quantify the population of RR galaxies using the SDSS complete sample. We conclude that the RR galaxies form a unique but rare population, accounting for only a small fraction of the massive quiescent galaxy population. We discuss the formation scenarios of the RR galaxies.

Keywords: Neutral hydrogen clouds (690), Galaxy dark matter halos (1880)

1. INTRODUCTION

In current theory of structure formation, galaxies form at the center of dark matter halos through gas cooling and condensation (White & Rees 1978; Mo et al. 2010). As the dominant component of cold gas, the atomic hydrogen (HI) reservoir is expected to play a vital role in regulating the rise and fall of star formation in galaxies. In fact, the HI surface mass density in low-redshift galaxies has been found to tightly correlate with the surface density of their star formation rate (SFR), known as the Kennicutt-Schmidt law (Kennicutt 1998). In addition, large surveys of multiband imaging and spectroscopy as

well as HI emission at 21cm have revealed strong correlations between the HI-to-stellar mass ratio (M_{HI}/M_{*}) and the optical and UV properties of galaxies, with lower HI mass fractions in galaxies with redder colors, lower SFRs and higher stellar mass densities (e.g. Haynes & Giovanelli 1984; Kannappan 2004; Zhang et al. 2009; Catinella et al. 2010; Huang et al. 2012; Li et al. 2012; Brown et al. 2015; Catinella et al. 2018; Li et al. 2022; Liu et al. 2023). In particular, it has been widely accepted that the cessation of star formation in a galaxy must be associated with the reduction of its HI reservoir. In a recent review, Saintonge & Catinella (2022) concluded that there is no evidence for a significant population of passive galaxies with HI reservoirs comparable to those of star-forming galaxies, based on extensive analyses of the extended GALEX Arecibo SDSS survey (xGASS; Catinella et al. 2010; Catinella et al. 2018).

Corresponding author: Xiao Li & Cheng Li
xli27938@gmail.com

cli2015@tsinghua.edu.cn

On the other hand, given the large scatter of the HI scaling relations found in previous studies, typically $0.2 - 0.3$ dex in $\log_{10}(M_{\text{HI}}/M_*)$, one can expect that some galaxies will deviate significantly from the average relations. Studies of galaxies with HI anomalies should in principle provide insights into the physical processes that drive gas-related star formation and quenching, and probably also cosmological models (e.g. [Peebles 2022](#)). In this regard, there has been a rich history of studies on the HI content of early-type galaxies (ETGs; e.g. [Knapp et al. 1985](#); [Wardle & Knapp 1986](#); [Bregman et al. 1992](#); [Morganti et al. 2006](#); [di Serego Alighieri et al. 2007](#); [Grossi et al. 2009](#); [Serra et al. 2012](#); [Young et al. 2014](#)). The ATLAS^{3D} HI survey ([Serra et al. 2012](#)) obtained resolved HI observations for a volume-limited sample of 166 nearby ETGs selected from ATLAS^{3D} ([Cappellari et al. 2011](#)), detecting significant HI in $\sim 10\%$ of all the ETGs inside the Virgo cluster and $\sim 40\%$ of those outside. In addition, the HI discs of these galaxies are found to have much larger sizes than their optical parts, as well as much lower HI column densities than what was found typically in spiral galaxies ([Serra et al. 2012, 2014](#)). Although with large HI detection rates, ETGs usually have low HI mass fractions as expected from their relatively low SFRs.

Some other attempts have been made to search for HI content in E+A, or post-starburst (PSB) galaxies (e.g. [Chang et al. 2001](#); [Buyle et al. 2006, 2008](#); [Zwaan et al. 2013](#); [Pracy et al. 2014](#)), a rare population of galaxies that are believed to have their star formation recently shut down, with no/little H α emission but strong high-order Balmer absorption indicative of young stars. [Zwaan et al. \(2013\)](#) detected HI emission in a high fraction (6/11) of E+A galaxies selected from the 2dF Galaxy Redshift Survey (2dFGRS; [Colless et al. 2001](#)) and the Sloan Digital Sky Survey (SDSS; [York et al. 2000](#)). A followup by [Pracy et al. \(2014\)](#) obtained integral field spectroscopy (IFS) for two E+A galaxies with HI emission, finding them to be consistent with a post-starburst population only in the central region, with the outer regions of both galaxies presenting strong optical emission lines. It is thus not surprising for a large fraction of the E+A galaxies in [Zwaan et al. \(2013\)](#) to have HI gas extending to large radii.

There have also been many observational studies to search “HI-excess” galaxies (e.g. [Wang et al. 2013](#); [Huang et al. 2014](#); [Lee et al. 2014](#); [Lemonias et al. 2014](#); [Wang et al. 2015](#); [Geréb et al. 2016](#); [Lutz et al. 2017](#); [Geréb et al. 2018](#); [Lutz et al. 2018, 2020](#); [Randriamampandry et al. 2021](#); [Zasov & Zaitseva 2022](#)), which are usually strongly star-forming galaxies with late-type morphologies, identified as extreme outliers to the scal-

ing relation between HI and stellar content of galaxies. Compared to galaxies with normal HI contents, these galaxies are found to have much larger HI disks and lower HI surface densities, but similar optical sizes and radial distributions of the gas-phase metallicity. [Geréb et al. \(2018\)](#) obtained HI resolved maps and optical spectra for four HI-excess galaxies, and found that the HI disk and stellar bulge are counter-rotating in one of the galaxies, suggesting external origin of the excessive HI. However, [Lutz et al. \(2020\)](#) found no indication for counter-rotation in any of their HI-excess galaxies. By examining the star formation activity and HI kinematics, [Lutz et al. \(2018\)](#) suggested that these galaxies stabilize their large HI discs by their higher-than-average baryonic specific angular momentum, likely inherited from the high spin of their host dark halos.

Several recent studies have focused on HI-rich galaxies with suppressed SFRs ([Lemonias et al. 2014](#); [Parkash et al. 2019](#); [Guo et al. 2020](#); [Wang et al. 2022a](#); [Sharma et al. 2023](#)). [Lemonias et al. \(2014\)](#) selected a parent sample of 258 HI-rich galaxies from the Arecibo Legacy Fast Arecibo L-band Feed Array Survey (ALFALFA; [Giovannelli et al. 2005](#); [Haynes et al. 2018](#)), defined as the top 5% fraction in the distribution of the HI mass-to-stellar mass ratio. From this parent sample, 20 massive and low-sSFR galaxies with $\log_{10}(M_*/M_\odot) > 10.6$, $\log_{10}(\text{sSFR}) < -10.75$ and $b/a > 0.5$ were selected for followup observations with the Very Large Array (VLA). [Guo et al. \(2020\)](#) analyzed a sample of 279 massive red spirals with $M_* > 10^{10.5} M_\odot$ and red colors defined by $u - r$, and found 74/166 in the ALFALFA catalog to have HI detections. [Wang et al. \(2022a\)](#) obtained followup HI observations with the Five-hundred-meter Aperture Spherical radio Telescope (FAST; [Nan 2006](#); [Jiang et al. 2020](#)) for the remaining 113 massive red spirals from [Guo et al. \(2020\)](#), detecting HI in 75 of them. [Parkash et al. \(2019\)](#) and [Sharma et al. \(2023\)](#) selected HI-detected galaxies from HI Parkes All-Sky Survey Catalog (HICAT; [Meyer et al. 2004](#)) and the HI-MaNGA program ([Stark et al. 2021](#)), respectively, both using a mid-infrared color selection of $W2 - W3 < 2.0$ to select galaxies with $\text{sSFR} < 10^{-10.4} \text{yr}^{-1}$. [Sharma et al. \(2023\)](#) further applied a selection of $M_{\text{HI}} > 10^{9.3} M_\odot$.

The high detection rates of HI emission in galaxies with suppressed SFRs appear to challenge the well-established correlation of low star formation with low HI gas mass (see the review by [Saintonge & Catinella 2022](#), and references therein). Based on an analysis of the data from SDSS, xGASS and ALFALFA, [Zhang et al. \(2019\)](#) claimed that nearly all massive quiescent disk galaxies in the local Universe have a large HI reservoir, similar to star-forming galaxies of similar masses. This claim

was attributed by Cortese et al. (2020) to the use of aperture-corrected SFR estimates from the MPA/JHU SDSS catalog (Brinchmann et al. 2004), which do not provide a fair representation of the global SFR of HI-rich galaxies with extended star-forming discs. In a recent study, Li et al. (2023) made careful image analysis and obtained reliable SFR estimates for a sample of nearby galaxies, and they confirmed that the MPA/JHU SDSS catalog indeed significantly overestimates the SFRs for low-SFR galaxies. For massive red spirals, Zhou et al. (2021) and Wang et al. (2022a) pointed out that many of the galaxies selected by optical color $u - r$ in Guo et al. (2020) are actually green or even blue in $\text{NUV} - r$, the NUV -to-optical color index.

In this work, we attempt to identify a sample of “red but HI-rich” (RR) galaxies, in a way that differs from previous studies. First, we make use of three existing HI surveys/catalogs to maximize our sample size. These include xGASS, ALFALFA and HI-MaNGA. Second, we use $\text{NUV} - r$ as a reliable indicator of the global star formation status of a galaxy, and we use the commonly adopted color criterion of $\text{NUV} - r > 5$ to select truly red, thus fully-quenched galaxies. As we will show, this color index works better than both the optical color $u - r$ and the mid-infrared color $W2 - W3$. Third, we use a *complete* (volume-limited) sample of galaxies selected from the SDSS as a reference, and we identify our RR galaxies as outliers located outside the 95% contour of the SDSS galaxy distribution in the HI mass fraction versus $\text{NUV} - r$ space. For each of the SDSS galaxies, we have estimated an HI mass based on Bayesian inferences of a number of optical properties, a technique developed in our previous work (Li et al. 2022). With the help of the SDSS sample, we are able to quantify the existence and rareness of the RR galaxies as a population. Finally, we use SFRs from both the MPA/JHU SDSS catalog and the GSWLC (Salim et al. 2018). The latter applied SED fitting to photometry from UV to IR, expected to provide more reliable estimates particularly for low-SFR galaxies (e.g. Li et al. 2023). As we will show, the RR sample selected this way is unique compared to all the previous similar samples. We will compare the optical properties and local environment of the RR galaxies with control samples of HI-normal galaxies of similar mass and color.

The paper is organized as follows. In section 2 we introduce the data used in this analysis. We present our results in section 3 and discussion in section 4. We summarize our main results in section 5. Throughout this paper, we assume a Λ CDM cosmology with $\Omega_M = 0.3$, $\Omega_\Lambda = 0.7$, and $h = 0.7$. We denote \log_{10} as log for simplicity.

2. DATA AND SAMPLE SELECTION

2.1. HI galaxy surveys

We use HI observations of nearby galaxies from three surveys: ALFALFA, xGASS, and the HI-MaNGA program.

ALFALFA is a blind survey of HI 21 cm emission in galaxies over 7000 deg^2 of the sky and up to redshift $z \sim 0.06$. Two sky areas are covered by ALFALFA: one in the northern Galactic hemisphere and one in the southern Galactic hemisphere. The final ALFALFA catalog, the $\alpha.100$ catalog contains $\sim 31,500$ extragalactic HI line sources out to $z \sim 0.06$ (Haynes et al. 2018). For each source, a category code is assigned according to data quality, with “code 1” for sources of the highest data quality and “code 2” for sources with lower data quality but a high likelihood to be true. There are 25,434 sources of “code 1” and 6,068 sources of “code 2”. In this work we use both categories.

The xGASS was accomplished also with the Arecibo telescope for targeted galaxies that are randomly selected from a parent sample of galaxies located in the overlapping region among SDSS data release 6 (Adelman-McCarthy et al. 2008), GALEX Medium Imaging Survey (Martin et al. 2005), and the ALFALFA survey footprint. The whole program was separated into two successive phases resulting in two complementary surveys: GASS and xGASS. The GASS obtained HI observations for a sample of galaxies with redshift $0.025 < z < 0.05$ and a flat stellar mass distribution in the range $10^{10} M_\odot < M_* < 10^{11.5} M_\odot$, down to a uniform limit of $\sim 1.5\%$ in HI-to-stellar mass ratio. The xGASS extends the stellar mass limit of the survey down to $M_* \sim 10^9 M_\odot$, by further observing a sample of galaxies with $10^9 M_\odot < M_* < 10^{10.2} M_\odot$ in the redshift range $0.01 < z < 0.02$. In this work we use the xGASS representative sample constructed by Catinella et al. (2018), including 1,179 galaxies from GASS and xGASS.

The HI-MaNGA is an HI followup program for the SDSS-IV MaNGA survey (Bundy et al. 2014). The MaNGA galaxies with $cz < 15000 \text{ km s}^{-1}$ and located outside the ALFALFA footprint are observed with the Green Bank telescope, down to a rms noise comparable to the ALFALFA survey (around 1.5 mJy at a velocity resolution of 10 km s^{-1}). The final HI-MaNGA catalog contains 6,358 MaNGA galaxies.

2.2. The SDSS galaxy sample

To compare our HI-selected samples with the general galaxy population, we have selected a volume-limited sample of galaxies out of the New York University Value-Added Galaxy Catalog (NYU-VAGC), constructed by Blanton et al. (2005) from the SDSS spectroscopic

galaxy sample. This sample includes 69,296 galaxies with stellar masses $M_* > 10^9 M_\odot$ and spectroscopically-measured redshifts $0.02 < z < 0.05$.

2.3. Galaxy properties

For each galaxy in the HI surveys and the SDSS sample we have collected or measured the following properties:

- M_* : stellar mass from the NASA-Sloan Atlas¹ (NSA; Blanton et al. 2011), estimated by Blanton & Roweis (2007) by performing a spectral energy distribution (SED) fitting to SDSS photometry assuming a Chabrier stellar initial mass function (Chabrier 2003).
- $NUV - r$: color index defined by NUV and r -band absolute magnitudes provided in NSA, both K -corrected and measured with an elliptical Petrosian model, but based on the GALEX and SDSS images, respectively.
- σ_{NUV-r} : error of $NUV - r$, calculated through error propagation based on the inverse variance of the NUV and r band absolute magnitudes in the NSA.
- R_{50} and R_{90} : the radii containing, respectively, 50% and 90% of the elliptical Petrosian flux in r band, in units of kpc, taken from NSA.
- R_{90}/R_{50} : the concentration index characterizing the degree of light concentration in the r band.
- $\mu_* \equiv M_*/(2\pi R_{50}^2)$: surface stellar mass density in units of $M_\odot \text{ kpc}^{-2}$.
- D_{4000} : the spectral break at 4000\AA taken from the MPA/JHU SDSS catalog², measured from the SDSS single fiber spectroscopy following the definition introduced by Balogh et al. (1999).
- σ_* : central stellar velocity dispersion taken from the MPA/JHU SDSS catalog, in units of km/s.
- SFR: total star formation rate in units of $M_\odot \text{ yr}^{-1}$. We use two SFR estimates: one from the GSWLC catalog derived by Salim et al. (2018) through SED fitting to the photometry ranging from UV to IR, and the other from the MPA/JHU catalog derived by Brinchmann et al. (2004) based on SDSS spectroscopy. The Chabrier IMF is assumed in both

cases. Unless otherwise stated we will use the GSWLC-based SFR.

- $s\text{SFR} \equiv \text{SFR}/M_*$: specific star formation rate. The GSWLC-based SFR is used unless otherwise stated.
- B/T : bulge-to-total luminosity ratio, taken from Meert et al. (2015).
- T-type: galaxy morphological type provided by Domínguez Sánchez et al. (2018). Generally, galaxies with T-type < 0 (T-type > 0) correspond to early-type (late-type) morphologies in the Hubble sequence.
- P_{merger} : probability of being a merger or projected pair taken from Domínguez Sánchez et al. (2018), based on the model trained by the Galaxy Zoo 2 catalog (GZ2; Willett et al. 2013).
- P_{bar} : probability of having a galactic bar taken from Domínguez Sánchez et al. (2018). Two estimates are provided for each galaxy, $P_{bar,GZ2}$ and $P_{bar,N10}$, based on two different models trained by the GZ2 catalog and the catalog of Nair & Abraham (2010), respectively. We use both estimates in our work.
- $(g - r)_{R_{50}}$ and $(g - r)_{0.5R_{50}}$: color index $g - r$ measured at R_{50} and $0.5R_{50}$, based on the g and r band images from the DESI Legacy Survey³.
- $\Delta_{g-r} \equiv (g - r)_{R_{50}} - (g - r)_{0.5R_{50}}$: radial gradient in $g - r$.

In addition to the optical properties listed above, we have estimated the HI gas mass for each galaxy using the estimator developed in Li et al. (2022). In short, the estimator uses a linear combination of four photometric parameters to estimate the HI-to-stellar mass ratio (M_{HI}/M_*) of galaxies, with coefficients of the parameters constrained using Bayesian inferences of real HI data from the xGASS. Extensive tests show that the estimator can provide unbiased HI mass for optically-selected samples like SDSS. The reader is referred to Li et al. (2022) for more details about the tests and applications of the estimator. The HI mass distribution of the SDSS volume-limited sample provides a *predicted* reference, to be compared below with samples selected from the HI surveys.

¹ <http://nsatlas.org>

² <https://wwwmpa.mpa-garching.mpg.de>

³ <https://www.legacysurvey.org>

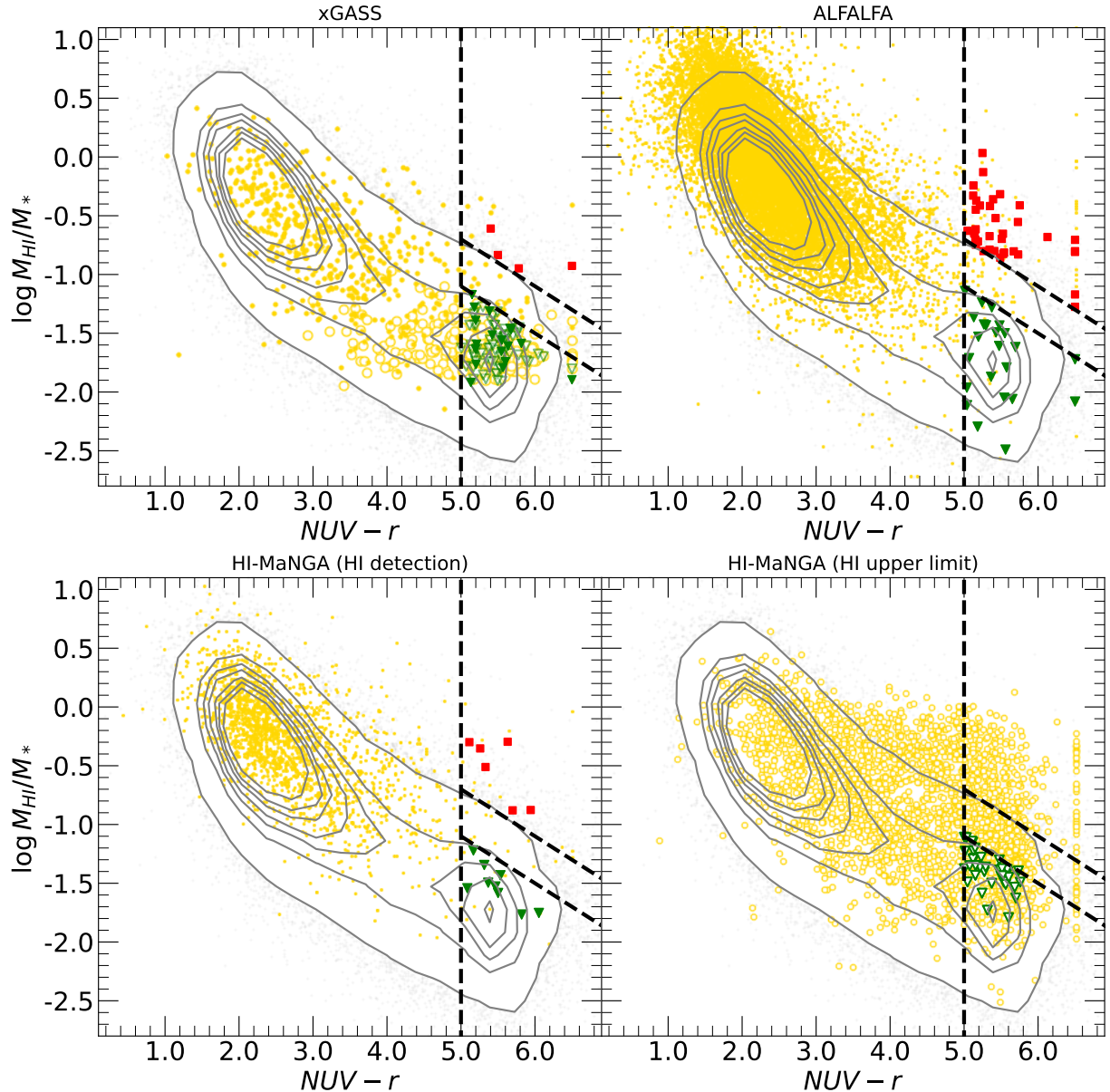


Figure 1. Sample selection. The gold solid dots represent the parent sample of all galaxies with HI observation from xGASS (upper-left), ALFALFA (upper-right), and HI-MaNGA (lower-left for detections and lower-right for upper limits), after removing potentially confused galaxies and galaxies with $\sigma_{\text{NUV}-r} > 0.3$. Solid and open symbols represent HI detections and upper limits separately. Galaxies included in the final RR and RN sample are shown as red squares and green triangles, respectively. The color is set to $\text{NUV} - r = 6.5$ for a few galaxies which have large uncertainties in NUV (see text in subsection 2.4 for details). The grey contours represent the SDSS volume-limited sample, of which the HI mass of each galaxy is predicted by the estimator developed by Li et al. (2022). The outermost contour includes 95% of the total sample.

2.4. Selection of red HI-rich galaxies

Figure 1 shows $\log_{10} M_{\text{HI}}/M_*$ versus $\text{NUV} - r$, for the three HI surveys and the SDSS volume-limited galaxy sample. The SDSS sample is plotted as grey contours and repeated in every panel. Galaxies in different HI surveys are shown as colored symbols in different panels. In each panel, HI detections are plotted as solid dots, while upper limits are plotted as open circles. For

clarity the HI-MaNGA sample is divided into two panels, one for HI detections and one for upper limits. The anticorrelation between HI mass fraction and color, and the color bimodality can be clearly seen in the SDSS sample. All the current HI surveys are biased for relatively HI-rich and blue galaxies due to limited survey depths. Although the smallest in sample size, the xGASS is the deepest and thus most complete among all the surveys

Table 1. Basic properties of the RR sample: source id, right ascension, declination, redshift, stellar mass from the NSA, $\text{NUV} - r$ color index (those assigned a fixed $\text{NUV} - r$ are shown as ≥ 6.50), Petrosian 50% and 90% radii in r band, SFR taken from GSWLC and MPA/JHU (those not matched to these catalogs are denoted as $-$), HI mass, source of HI mass (0:ALFALFA, 1:xGASS, 2:HI-MaNGA)

id	ra	dec	z	$\log_{10} M_*$	$\text{NUV} - r$	$\log_{10} R_{50}$	$\log_{10} R_{90}$	$\log_{10} \text{SFR}_{\text{GSWLC}}$	$\log_{10} \text{SFR}_{\text{MPA}}$	$\log_{10} M_{\text{HI}}$	HI src
				$[M_{\odot}]$	$[\text{mag}]$	$[\text{kpc}]$	$[\text{kpc}]$	$[M_{\odot} \text{ yr}^{-1}]$	$[M_{\odot} \text{ yr}^{-1}]$	$[M_{\odot}]$	
0	28.6710	-0.1434	0.0185	10.68	5.33	0.54	1.06	-1.37	-1.54	10.17	2
1	19.4449	13.3234	0.0479	10.25	5.26	0.33	0.86	-1.87	-1.22	10.12	0
2	128.1644	53.2332	0.0430	10.30	5.11	0.39	0.88	-1.99	-0.98	10.00	2
3	52.3316	-6.4779	0.0420	10.20	5.26	0.23	0.67	-1.02	-1.17	9.85	2
4	149.4660	1.7554	0.0320	10.54	5.70	0.39	0.83	-2.05	-1.23	9.66	2
5	179.6394	1.3700	0.0485	10.32	5.73	0.26	0.71	-1.86	-1.39	9.77	0
6	142.0508	3.4084	0.0116	10.31	5.53	0.11	0.62	-2.25	-1.66	9.48	0
7	153.3518	5.0255	0.0464	10.05	5.40	0.14	0.55	-2.05	-1.38	9.44	1
8	221.8548	3.4411	0.0274	10.42	5.39	0.29	0.82	-1.37	-1.29	10.06	0
9	333.9182	13.8821	0.0246	10.09	5.15	0.30	0.71	-0.65	-1.13	9.38	0
10	340.1470	13.9773	0.0367	10.24	5.35	0.29	0.78	-0.78	-1.31	9.82	0
11	198.3802	5.9155	0.0486	10.98	5.43	0.73	1.15	-1.32	-0.95	10.46	0
12	163.0032	50.8430	0.0260	10.20	5.94	0.30	0.73	-2.58	-1.43	9.32	2
13	159.7155	5.6701	0.0283	10.26	5.63	0.33	0.77	-2.50	-1.33	9.96	2
14	139.6306	6.8732	0.0393	10.38	5.78	0.26	0.75	-0.68	-1.29	9.44	1
15	242.0909	26.5281	0.0540	10.56	6.50	0.33	0.83	-1.10	-1.05	9.76	0
16	249.3657	26.2047	0.0522	10.81	6.50	0.81	1.25	-1.21	-1.24	10.10	0
17	215.6282	11.3049	0.0164	10.36	5.34	0.10	0.61	-1.49	-1.80	9.57	0
18	223.2200	12.3523	0.0299	10.50	5.73	0.32	0.82	-1.94	-1.46	9.67	0
19	155.5138	13.7695	0.0186	10.18	5.14	0.36	0.88	-2.92	-1.42	9.53	0
20	226.2269	7.2125	0.0560	10.09	5.25	0.25	0.67	-1.52	-1.45	10.12	0
21	216.0679	33.6126	0.0223	10.38	5.26	0.24	0.68	-1.95	-1.62	9.58	0
22	149.7208	31.6203	0.0214	10.47	5.49	0.37	0.88	-2.19	-1.36	9.61	0
23	178.1931	32.3099	0.0317	10.44	5.16	0.27	0.78	-1.93	-0.98	9.82	0
24	205.5474	29.8956	0.0272	10.22	5.16	0.02	0.47	-1.56	-1.59	9.77	0
25	208.8057	25.2164	0.0360	10.22	5.49	0.31	0.80	-1.42	-1.30	9.90	0
26	227.1210	21.9477	0.0206	10.56	5.34	0.45	0.94	-2.04	-1.60	9.89	0
27	246.7624	16.3822	0.0154	10.46	6.50	0.52	0.97	-1.48	-1.25	9.65	0
28	142.5893	25.2524	0.0587	10.95	5.41	0.71	1.24	-0.77	-1.23	10.15	0
29	162.3703	26.0396	0.0217	10.36	5.51	0.16	0.66	-2.16	-1.45	9.66	0
30	155.4069	21.6873	0.0392	10.53	5.16	0.36	0.83	-0.51	-1.26	9.78	0
31	120.0874	11.3194	0.0149	10.25	6.13	0.27	0.68	-1.40	-1.90	9.57	0
32	132.6887	11.8108	0.0297	10.41	5.50	0.20	0.66	-	-1.36	9.58	1
33	241.2004	14.1289	0.0338	10.87	5.12	0.42	0.91	-1.71	-1.09	10.54	0
34	240.8469	14.5245	0.0357	10.52	5.19	0.29	0.77	-1.40	-1.28	9.80	0
35	150.2089	13.7370	0.0325	10.20	5.16	0.09	0.60	-1.90	-1.51	9.83	0
36	171.2433	7.6274	0.0415	10.75	5.05	0.48	1.01	-	-	10.12	0
37	16.5919	6.2825	0.0352	10.87	5.13	0.48	0.98	-	-	10.63	0
38	23.6161	19.8206	0.0357	10.87	5.14	0.49	0.96	-	-	10.22	0
39	45.1559	35.1691	0.0169	10.77	6.50	0.58	0.98	-	-	9.50	0
40	359.4070	18.1909	0.0260	10.53	5.54	0.24	0.71	-	-	9.72	0
41	1.4582	17.3534	0.0181	10.17	5.21	0.04	0.55	-	-	9.76	0
42	24.0705	23.2281	0.0343	10.93	5.67	0.59	1.11	-	-	10.13	0
43	329.8712	15.2784	0.0252	10.50	5.53	0.23	0.73	-	-	9.85	0
44	37.0733	26.3125	0.0174	10.63	5.75	0.26	0.80	-	-	10.22	0
45	344.9648	26.0331	0.0332	11.15	6.50	0.93	1.34	-	-	9.98	0
46	207.9975	13.9675	0.0366	10.89	6.50	0.83	1.28	-0.21	0.04	9.96	1

considered here. However, even the xGASS lacks all the red galaxies with $M_{\text{HI}}/M_* \lesssim 1.5\%$. Interestingly, the shallower ALFALFA survey has detected HI for a (small) number of low- z galaxies with red colors ($\text{NUV} - r > 5$)

and low gas fraction because of their relatively high HI masses, covering nearly the same range of M_{HI}/M_* as predicted for the red galaxy population in the SDSS.

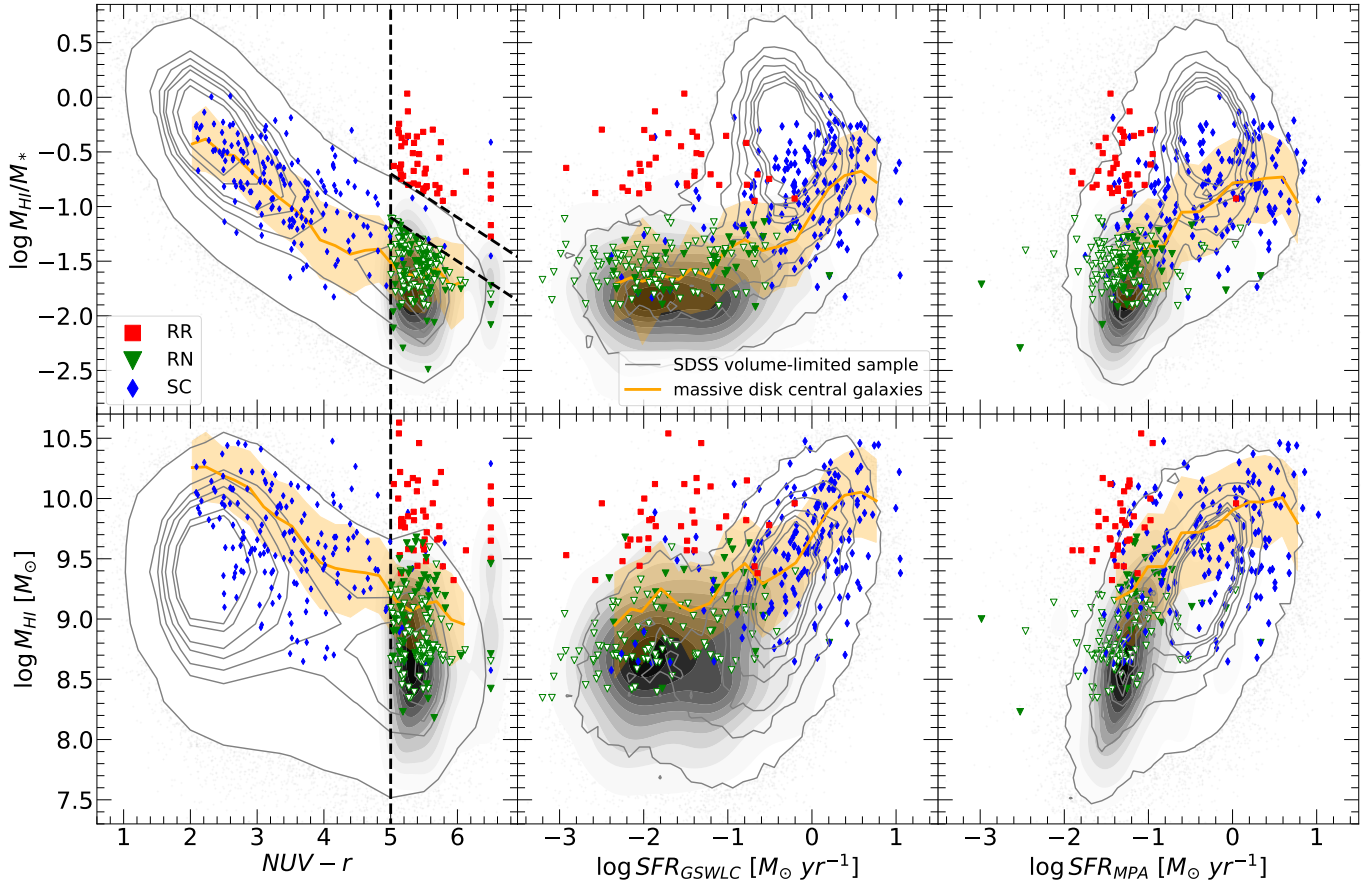


Figure 2. Diagrams of M_{HI}/M_* (the top row) and M_{HI} (the bottom row), versus $NUV - r$ (the left column) and SFRs (with SFRs from GSWLC in the middle column, and SFRs from the MPA/JHU catalog in the right column). The RR, RN, and SC galaxies are shown as red squares, green triangles, and blue diamonds, with solid and open symbols for HI detections and non-detections (upper limits) separately. The color is set to $NUV - r = 6.5$ for a few galaxies which have large uncertainties in NUV (see text in subsection 2.4 for details). The grey contours represent the SDSS volume-limited sample, of which the HI mass of each galaxy is predicted by the estimator developed by Li et al. (2022). The outermost contour includes 95% of the total sample. The filled grey contours represent the CSC sample. The orange solid line and the shaded region show the median and the $1 - \sigma$ scatter of the HI-to-stellar mass ratio for massive disk central galaxies.

We select red but HI-rich (RR) galaxies from the three HI surveys by requiring them to have substantially red colors, $NUV - r > 5$ and $\sigma_{NUV-r} < 0.3$, as well as outstandingly high HI masses, $\log_{10}(M_{\text{HI}}/M_*) + 0.4 \times (NUV - r) - 1.3 > 0$. The two criteria are indicated by the vertical and upper-right dashed lines in Figure 1. The latter criterion is manually determined, and it roughly matches the 95% percentile contour of the SDSS galaxy distribution. We consider only HI detections when identifying RR galaxies, to make sure their HI mass fractions meet our requirement. For comparison, we have selected a sample of red and HI-normal (RN) galaxies with the same criteria in color and color error as adopted for RR, but requiring the HI-to-stellar mass ratio to fall below the 75% percentile contour, or specifically $\log_{10}M_{\text{HI}}/M_* + 0.4 \times (NUV - r) - 0.9 < 0$, as indicated by the lower dashed line plotted to the right

of each panel. We consider both HI detections and upper limits when selecting RN galaxies. This is because a galaxy must fall below the lower dashed line if its HI upper limit is already below this line. There are a small number of galaxies with unusually red colors ($NUV - r \gg 6.5$) due to their extremely large values of NUV magnitude with large uncertainties. We have visually examined their NUV images and found them to be truly faint in NUV. In order to include them in our analysis, we assign them a fixed color index of $NUV - r = 6.5$, the reddest color that can be reached by a simple stellar population (SSP) in current stellar population models (e.g. Bruzual & Charlot 2003). We apply the same criteria as above to select these galaxies into the RR or RN sample. In addition, we require all the selected RR and RN galaxies to not be confused with neighboring galaxies located in the same beam. We identify galaxies free

of confusion by requiring `HIconf_flag=0` for those from xGASS, and `conf_prob<0.1` for those from HI-MaNGA. For those from ALFALFA, we require them to have no neighboring galaxies within an angular radius of $3.5'$ and a radial velocity separation of 600 km s^{-1} . Finally, we visually examine the DESI image of all the selected galaxies, and exclude the edge-on galaxies with obvious dust lanes which could be intrinsically blue but reddened by dust attenuation.

With these restrictions we end up with 47 RR galaxies (37 from ALFALFA, 4 from xGASS and 6 from HI-MaNGA), as well as 573 RN galaxies (43 from ALFALFA, 237 from xGASS and 293 from HI-MaNGA). The basic properties of the RR sample are listed in [Table 1](#). In order to take care of the mass dependence when comparing the RR and RN samples, we further trim the RN sample so that its M_* distribution is the same as the RR sample. This yields a final sample of 154 RN galaxies, with 23 from ALFALFA, 80 from xGASS and 51 from HI-MaNGA. The RR and RN galaxies are highlighted in red and green color in [Figure 1](#), respectively. Note that the RN sample is dominated by upper limits.

The upper-left panel of [Figure 2](#) displays the M_{HI}/M_* versus $\text{NUV} - r$ relation for the final samples of RR and RN galaxies. In addition to these two samples, we have selected a stellar mass-controlled (SC) sample of 177 galaxies from the xGASS, which has the same M_* distribution as the RR and RN samples but with no restrictions on the color and the HI mass fraction. The galaxies in the SC sample are plotted as blue diamonds. The lower-left panel plots the HI mass instead of the HI-to-stellar mass ratio as a function of $\text{NUV} - r$ for the same samples. In the middle and right panels we plot M_{HI}/M_* and M_{HI} as functions of SFR, using the SFR estimates from GSWLC and the MPA/JHU catalog, respectively.

The RR and RN galaxies are roughly separated at $M_{\text{HI}} \sim 10^{9.5} M_{\odot}$, and both samples are dominated by galaxies with low SFRs ($\log_{10} \text{SFR} \lesssim -1$) consistent with their red colors, for SFRs given by both GSWLC and MPA/JHU. When the GSWLC SFRs are used and at the low-SFR end ($\log_{10} \text{SFR} \lesssim -1$), the RN and SC samples appear to follow roughly the overall trend of the SDSS sample, where both the HI-to-stellar mass ratio and the total HI mass depend only weakly on the SFR, roughly at $\log_{10}(M_{\text{HI}}/M_*) \sim -1.8$ and $\log_{10}(M_{\text{HI}}/M_{\odot}) \sim 8.7$, respectively. At higher SFRs, the SC sample follows the M_{HI} -SFR relation of the SDSS sample, but is biased towards relatively low $\log_{10}(M_{\text{HI}}/M_*)$. This should be produced by the relatively high stellar masses of the SC sample at which the average SFR is reduced by galaxies from the quiescent sequence (see [Figure 3](#) below). When

the MPA/JHU SFRs are used and at the low-SFR end, the SDSS sample presents a clump-like distribution in the M_{HI}/M_* versus SFR relation and a positive correlation between M_{HI} and SFR, with a more limited SFR range and larger scatter in M_{HI}/M_* and M_{HI} than when the GSWLC SFRs are adopted. The distributions of the RR, RN and SC samples relative to the SDSS sample remain similar, however, regardless of the adopted SFR estimate.

One may worry that the RN sample is not substantially representative of the general population of red galaxies, as it is selected from the HI surveys but not directly from the parent SDSS sample. To address this possibility, we use the SDSS sample to construct another control sample (referred to as ‘‘CSC’’), which consists of 423 galaxies and is matched with the RR sample in both M_* and $\text{NUV} - r$. The distributions of the CSC sample are shown as filled grey contours in [Figure 2](#). As expected, the CSC sample well represents the underlying red population of the SDSS sample.

The majority of the RR galaxies are located beyond the 95% contour of the SDSS sample, suggesting that red galaxies with large amounts of HI gas are rather rare. In other words, red/quenched galaxies are mostly HI-poor, with only a small fraction having unusually large amounts of HI gas. In the next section we will compare the RR and RN samples in detail, aiming to figure out the origin of the high HI gas content of RR galaxies.

3. RESULTS

3.1. Optical properties

In [Figure 3](#) we examine the optical properties for the RR and RN samples, and compare with the SC sample and the SDSS volume-limited sample. We consider a variety of galaxy properties, each plotted in one panel as a function of $\log_{10} M_*$. In each panel, the RR, RN and SC galaxies are plotted as red squares, green triangles, and blue diamonds, respectively. The distribution of the SDSS sample is plotted as the background contours. The CSC sample is shown as the grey filled contours. A side panel is added to the right of each panel, showing the cumulative distribution of the corresponding property for the RR, RN, SC and CSC samples, respectively. Overall, the well-known galaxy bimodality can be clearly seen from the SDSS sample in many properties, e.g. $\text{NUV} - r$, SFR, D_{4000} , R_{90}/R_{50} , μ_* and the T-type. In all panels the RN sample shows similar distributions to the CSC sample, demonstrating that the RN sample is a representative subsample of the red galaxy population of their mass. The RR galaxies are limited to relatively high masses, with $M_* \gtrsim 10^{10} M_{\odot}$, a result that can be understood from their red colors. As can be

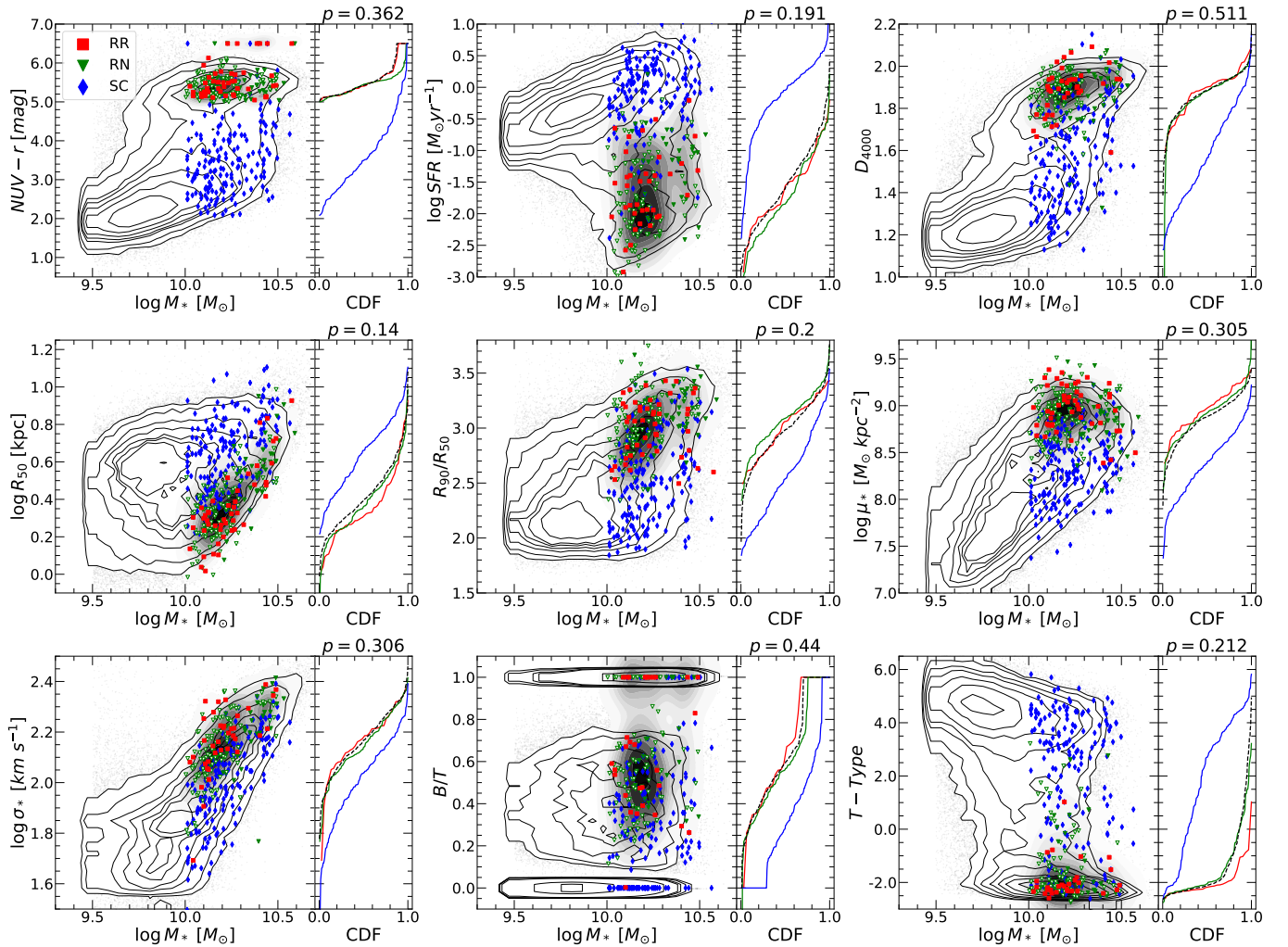


Figure 3. Galaxy properties as a function of stellar mass. The grey contours represent the SDSS volume-limited sample, of which the HI mass of each galaxy is predicted by the HI estimator (Li et al. 2022). In this figure, some galaxies have $NUV - r = 6.5$, this is not the observed value but set artificially (see subsection 2.4 for details). Solid/open markers represent HI detections/non-detections (upper limits). The red squares represent RR galaxies. The green downward triangles represent RN galaxies. The blue diamonds represent SC galaxies. The colored lines denote the normalized cumulative distribution of the y-axis galaxy properties (red for RR, green for RN, blue for SC, and black dashed for CSC). The grey filled contours represent the CSC sample. The p-value of the two-sample KS test conducted between the RR and the RN sample is indicated above each side panel.

seen from the color-mass diagram (the top-left panel), the general population of galaxies at $NUV - r > 5$ from the SDSS sample is predominantly massive.

We find that the RR and RN galaxies have similar distributions in all the properties considered. Both types of galaxies fall in the sequences of red (by selection) and quiescent galaxies with relatively low SFRs and old stellar populations as indicated by their high D_{4000} . The two types of galaxies are also similar in optical size (R_{50}) and structural properties (R_{90}/R_{50} and μ_*) at any given mass, with smaller sizes, more centrally concentrated light distributions and higher stellar mass densities in comparison to the general galaxy population. In addition,

they exhibit similarly high σ_* , high B/T and low T-type, all indicative of early-type morphologies.

In Figure 4 we further examine the merger probability (P_{merger}), the probabilities of hosting a galactic bar ($P_{\text{bar,GZ2}}$ and $P_{\text{bar,N10}}$), the $(g - r)$ color indices measured at R_{50} and $0.5R_{50}$, and the radial gradient of the color indices. For each property, we show both the differential and the cumulative distributions for the three samples: RR, RN and SC. The RR and RN samples show very similar distributions for all properties considered except $P_{\text{bar,N10}}$, which appears to be smaller in the RR sample on average. The different distributions of $P_{\text{bar,GZ2}}$ and $P_{\text{bar,N10}}$ may be produced by the differ-

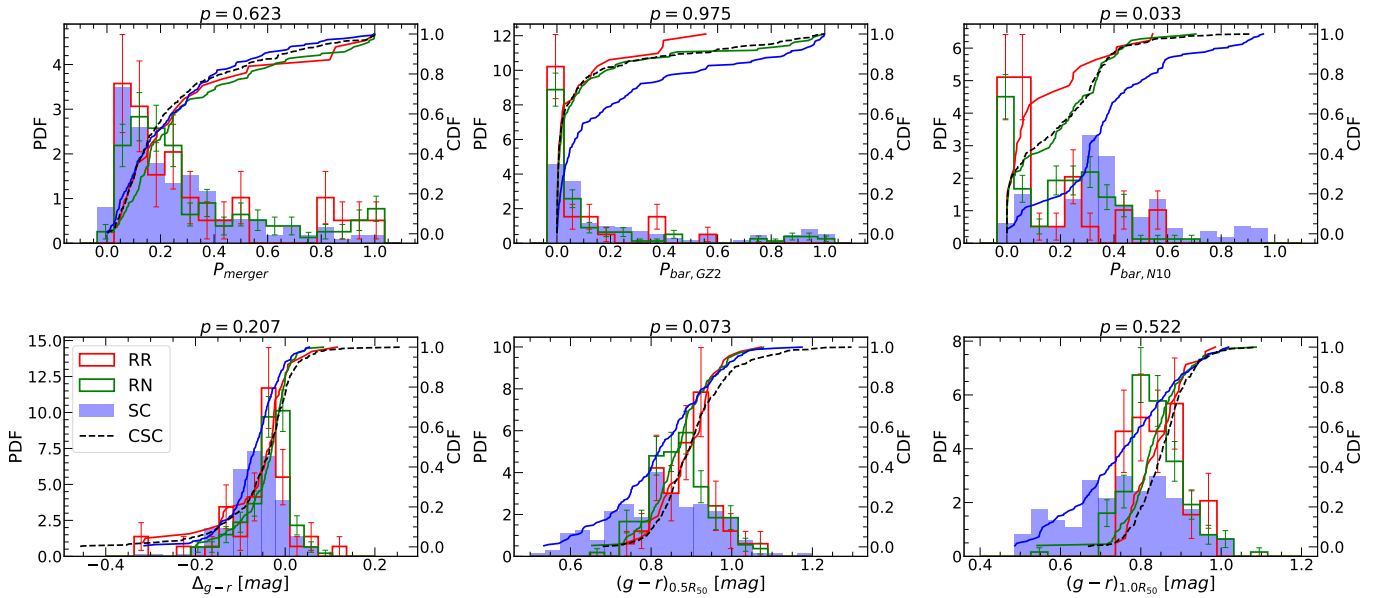


Figure 4. Probability distribution of galaxy properties. From top left to bottom right, the quantities in each panel are probability of being a merger or projected pair (P_{merger}), the probability of having bar signatures ($P_{bar,GZ2}$ and $P_{bar,N10}$), $g-r$ color gradient, $g-r$ at $0.5R_{50}$, and $g-r$ at R_{50} . The colored solid lines show the normalized cumulative distribution of the histograms with the same color. The p -value of the two-sample KS test conducted between the RR and the RN sample is indicated above each panel.

ent definitions of the two parameters, which can also be seen from their distributions in the SC sample. Given this difference, both the large p -value of the KS test using $P_{bar,GZ2}$ and the small p -value using $P_{bar,N10}$ should be taken with caution. We note that, however, nearly all the galaxies in both samples have $P_{bar} < 0.5$ indicative of no/weak bars, a result that is true for both $P_{bar,GZ2}$ and $P_{bar,N10}$. The majority of the RR and RN galaxies have low merger and bar probabilities, as well as negative color gradients, with $P_{merger} < 0.5$, $P_{bar,GZ2} < 0.2$, $P_{bar,N10} < 0.3$ and $\Delta_{g-r} < 0$ for $\sim 80\%$ of the sample galaxies. Nearly all the RR and RN galaxies have $(g-r) > 0.7$ at both $0.5R_e$ and R_e , consistent with their globally red colors. When compared to the SC sample, both the RR and RN samples are similar in P_{merger} and Δ_{g-r} , smaller in $P_{bar,GZ2}$ and $P_{bar,N10}$, and larger in $(g-r)$ at both R_{50} and $0.5R_{50}$.

Results as seen from Figure 3 and Figure 4 strongly suggest that, when compared to the RN galaxies of similar stellar masses, the RR galaxies have nothing special in any of the properties we have examined, including both the properties related to stellar populations and those related to galaxy structure, morphology and mergers. In fact, for each property we have performed a Kolmogorov-Smirnov (K-S) test for the RR and RN samples. The resulting p values are indicated above the panels in both figures, which confirm that the two samples are statistically drawn from the same parent sample.

3.2. Environments

The cold gas content of galaxies may be effectively reduced by environmental effects occurring in dense regions such as tidal stripping and ram-pressure stripping. These effects are expected to be more efficient for satellite galaxies than for central galaxies. To examine the central/satellite fractions of our galaxies and their environments at different scales, we use the SDSS galaxy group catalog of Yang et al. (2007) and the local environment density inferred from the density field reconstructed by Wang et al. (2016a), and we measure the projected two-point correlations and neighbor counts for our galaxy samples using the SDSS spectroscopic and photometric samples.

First of all, we cross match the RR, RN and SC samples with the group catalog constructed by Yang et al. (2007). A small number of our galaxies are not included in the group catalog, including 10, 16, and 3 galaxies from the RR, RN and SC samples, respectively. For these galaxies, we use the NSA to examine their neighboring galaxies, and we find that most of them (10/10, 14/16, 3/3 for the RR, RN and SC samples, respectively) are either the most massive or the only galaxy within a projected radius of 1 Mpc. We thus classify these “locally dominant galaxies” as centrals. The numbers and fractions of central/satellite galaxies in the three samples are listed in Table 2. We find that the majority of the RR galaxies are centrals in their host groups, with a very high central fraction of 89%, compared to 64%

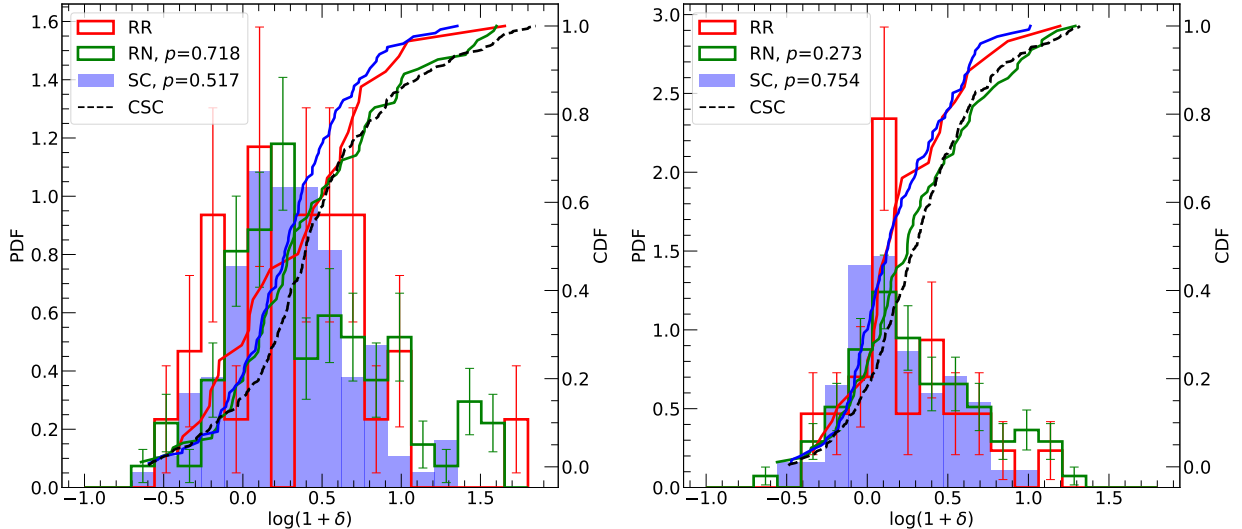


Figure 5. Histograms and cumulative distributions of $\log_{10}(1 + \delta)$, where δ is the local overdensity estimated at scales of 2 Mpc (left) and 4 Mpc (right) by Wang et al. (2016a). Results for the RR, RN, SC and CSC samples are plotted with different colors as indicated. For clarity, the histogram is not shown for the CSC sample. The p values from K-S tests are indicated by comparing the RR sample with the RN and SC samples.

and 76% in the RN and SC samples, respectively. According to the group catalog, we find the median halo mass of the RR galaxies is $M_h \sim 10^{12} h^{-1} M_\odot$, with 91% of the sample (compared to 71% and 84% for the RN and SC samples) to be hosted by relatively low-mass halos with $M_h < 10^{13} h^{-1} M_\odot$. For the RN galaxies, their host halos span a wide range of halo mass, with a median halo mass of $M_h \sim 10^{12.5} h^{-1} M_\odot$ and a significant fraction (18%) above $M_h \sim 10^{14} h^{-1} M_\odot$. This result clearly shows that, different from the RN galaxies, the RR galaxies are mainly central (or isolated) galaxies in relatively low mass halos, thus free of strong environmental effects and more capable of accreting and/or retaining their cold gas.

Table 2. Central/satellite numbers and fractions

sample	centrals or isolated	satellites	Total
RR	42(89%)	5(11%)	47
RN	98(64%)	56(36%)	154
SC	134(76%)	43(24%)	177

Next, we examine the three-dimensional overdensity of the local environment of our galaxies, $\delta \equiv \rho/\bar{\rho} - 1$, where ρ and $\bar{\rho}$ are the local and mean matter density, respectively. Taken from the ‘‘Exploring the Local Universe with the reConstructed Initial Density Field’’ project (ELUCID; Wang et al. 2016a), the matter density field can well reproduce the distribution of both galaxies and groups of galaxies in the local Universe as observed by

SDSS. Overdensities can be estimated at different scales by smoothing the density field with Gaussian kernels of different sizes. In Figure 5 we compare the distribution of the local overdensity as estimated at scales of 2 Mpc (left panel) and 4 Mpc (right panel) for different samples. At both scales, we find a trend for the RR galaxies to be located in relatively underdense regions compared to the RN sample, although the p -value of the two-sample Kolmogorov-Smirnov test shows that this difference is not very significant. The difference is more pronounced at 4 Mpc than at 2 Mpc, as indicated by the p -values.

We estimate two more statistics to further probe the environment of our galaxies over a wider range of spatial scales. The first statistic is the projected cross-correlation function (PCCF), $w_p(r_p)$, measured for each of our samples with respect to a reference sample of $\sim 5.3 \times 10^5$ galaxies from the SDSS spectroscopic survey. This statistic quantifies the clustering of galaxies over scales from a few $\times 10$ kpc up to a few $\times 10$ Mpc. The other statistic is the background-subtracted neighbor count, $N_c(< R_p)$, that is, the average number of neighboring galaxies within a projected distance R_p around the galaxies in our samples, as estimated in the SDSS photometric sample down to the r -band limiting magnitude of $r_{\text{lim}} = 21$ mag. The contribution by uncorrelated background galaxies is statistically estimated and subtracted. Detailed descriptions of the two statistics and tests/applications can be found in Li et al. (2006b, 2008a,b) and Wang & Li (2019). Figure 6 shows our measurements of w_p and N_c for the different sam-

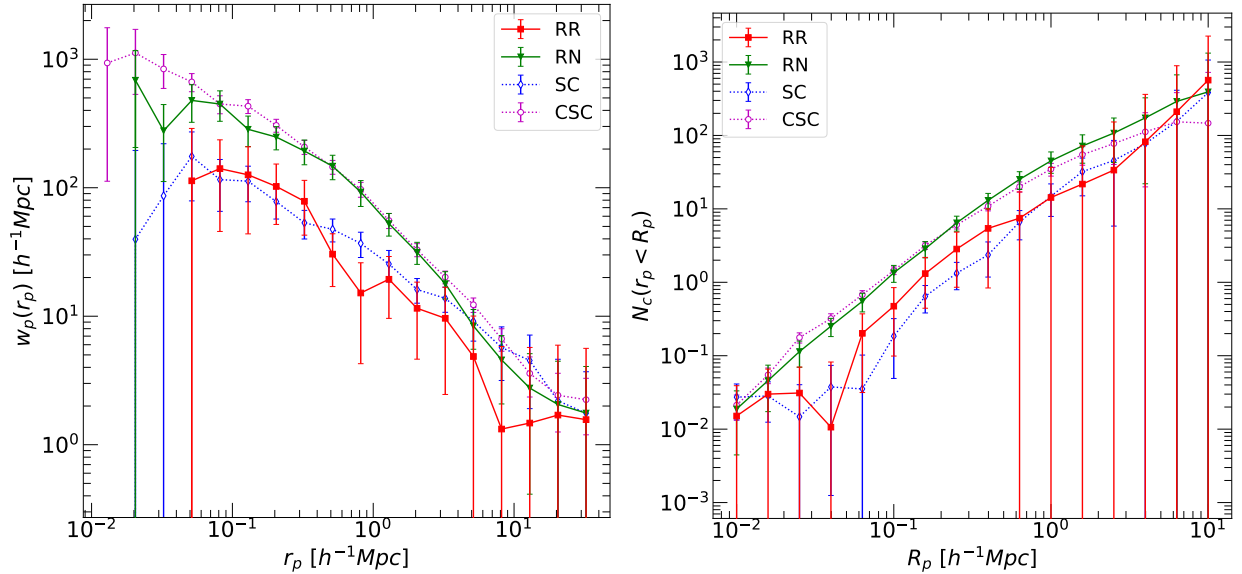


Figure 6. Measurements of projected cross-correlation functions with respect to the SDSS reference sample (upper) and background-subtracted neighbor counts in the SDSS photometric sample down to the r -band magnitude limit of $r_{\text{lim}} = 21$ (lower). Results for the different samples are plotted in different symbols/lines/colors, as indicated.

ples. First of all, for the CSC sample both the $w_p(r_p)$ and N_c measurements are in good agreement with those of the RN sample, demonstrating again that the RN sample is a random subset of the red population of their mass.

On scales larger than a few Mpc, the RN and SC samples present similar $w_p(r_p)$ amplitudes, implying similar dark matter masses of their host halos, while the RR sample shows weaker clustering (although with large errors). This result is consistent with both the smaller halo masses of the RR galaxies as found above from the SDSS group catalog and the lower local densities found at 4 Mpc from the reconstructed density field. On intermediate scales from a few Mpc down to ~ 100 kpc, the RR and SC samples show similar clustering amplitudes, which are significantly lower than that of the RN sample. The stronger clustering of the RN sample than the SC sample can be attributed to the different NUV $- r$ colors of the two samples. Previous studies of galaxy clustering have shown that, at scales below a few Mpc, red galaxies are more strongly clustered than blue galaxies of similar masses (e.g. Li et al. 2006a). Since the RR and RN samples are matched in both stellar mass and color, the weaker clustering of the RR sample at intermediate scales can be understood from the aforementioned higher fraction of central galaxies. As shown in Li et al. (2006b) and Wang & Li (2019), the dip in $w_p(r_p)$ at intermediate scales can well be reproduced by models in which a higher-than-average fraction of the galaxies are located at the centers of their host dark matter halos.

The N_c measurements present similar behaviors to $w_p(r_p)$. This is expected as the two statistics are closely related. Compared to $w_p(r_p)$, the N_c are measured with smaller errors on the smallest scales ($\lesssim 100$ kpc) thanks to the much deeper photometric sample. We see a trend for a dip at $R_p \sim 40 h^{-1}$ kpc as well as an upturn at smaller scales in the average number of close companions around the RR galaxies. This result might indicate some role of tidal interactions or mergers for RR galaxies. Large samples and more studies are needed to test this hypothesis.

3.3. HI-to-optical size ratio

Previous studies have revealed a tight relation between the HI disk size and HI mass for nearby galaxies (e.g. Wang et al. 2016b, and reference therein). The unusually high HI mass fractions of the RR galaxies thus imply large HI disk sizes relative to galaxies with normal HI contents, if we assume that different types of galaxies follow the same HI size-mass relation. We estimate the radius of the HI disk (R_{HI}) for each galaxy in our samples using the HI disk size-mass relation from Wang et al. (2016b), where R_{HI} is defined as the radius at which the surface HI mass density is equal to $1 M_{\odot} \text{pc}^{-2}$. The left-hand panel of Figure 7 shows the ratio of the estimated R_{HI} to the optical radius R_{90} as a function of stellar mass for the different samples of galaxies, with the side panel showing the histogram of R_{HI}/R_{90} of all the galaxies in each sample. As expected, the RR galaxies have the largest HI-to-optical size ratios with an average of $R_{\text{HI}}/R_{90} \sim 4$, compared to $R_{\text{HI}}/R_{90} \sim 1$ for the

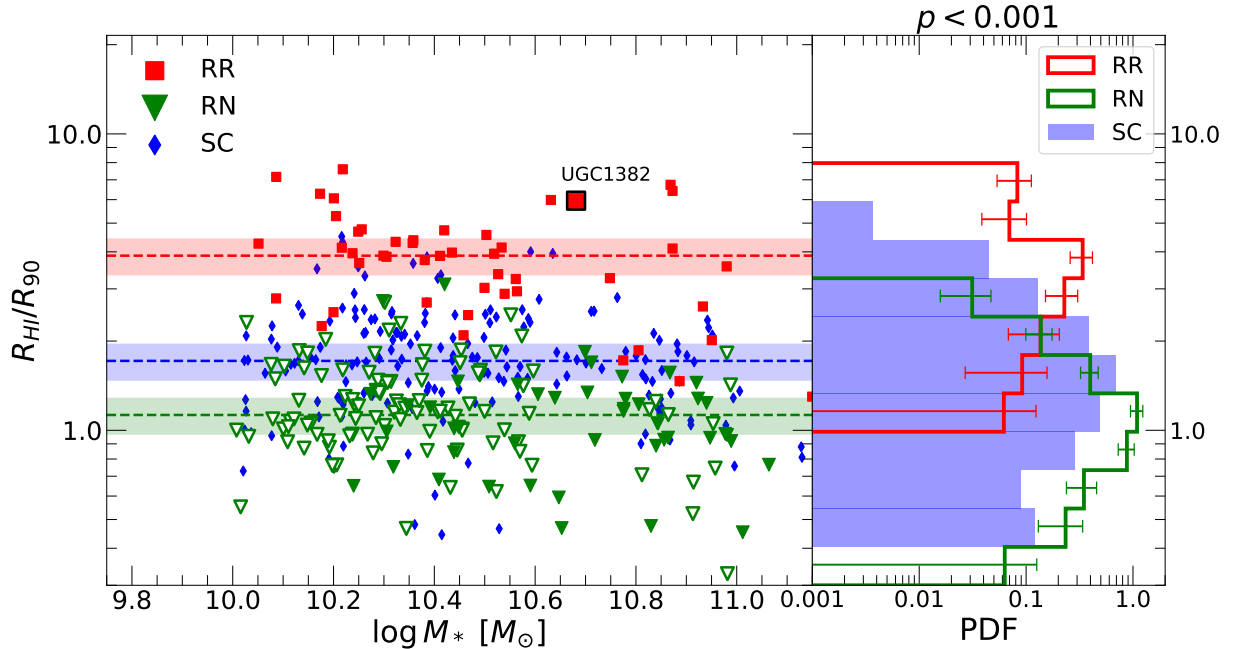


Figure 7. The HI-to-optical radius ratio as a function of stellar mass. The red squares represent the RR sample. The green triangles represent the RN sample. The blue diamonds represent the SC sample. Solid and open symbols represent HI detections and non-detections (upper limits) separately. The dashed lines show the median value of the HI-to-optical radius ratio for the three samples, with the shaded region indicating the uncertainty due to the scatter of the HI size-mass relation. The histograms show the normalized distribution of the HI-to-optical radius ratio. The p-value of the two-sample KS test conducted between the RR and the RN sample is indicated on top of the left panel. The red square is UGC 1382 (id=0 in Table 1), the only galaxy in the RR sample that has resolved HI observations available for measuring HI disk size (Hagen et al. 2016).

RN sample and $R_{\text{HI}}/R_{90} \sim 1.7$ for the SC sample. We see weak dependence on the stellar mass for all the three samples, although there is considerable scatter at fixed mass. Note that the RN sample is dominated by HI upper limits, and so the estimated HI sizes are also upper limits. This means that the HI disk of red galaxies with normal HI content is comparable or even smaller than their optical disk.

One of our RR galaxies, UGC 1382 (id=0 in Table 1) with resolved HI observations available for measuring HI disk size (Hagen et al. 2016) is highlighted in Figure 7 as a red square with black borders. This galaxy is above the average HI size-mass relation from Wang et al. (2016b), but with a deviation that is only slightly larger than the 3σ scatter. Although with only one galaxy, this result supports the assumption that the galaxies from different samples follow the same HI size-mass relation. This assumption is actually consistent with previous studies of resolved HI observations of nearby galaxies. For instance, using HI maps of nearby galaxies obtained from the Westerbork Synthesis Radio Telescope (WSRT), Wang et al. (2013) found that their “bluedisk” galaxies with unusually high HI mass fractions lie on the same HI mass versus HI size relation as the control galaxies with normal HI content, although

the former have much larger HI-to-optical size ratios, with R_{HI} extending to values as large as $\sim 100\text{kpc}$ for $M_{\text{HI}} \sim 2 \times 10^{10} M_{\odot}$ (see Figure 6 of their paper). Therefore, applying the same size-mass relation to estimate HI radii for different samples appears to be a reasonable choice for our analysis here, before large samples of resolved HI observation become available in the future.

4. DISCUSSION

4.1. Uniqueness of the RR galaxies

In this subsection we compare our RR sample with similar samples in previous studies. First, we consider the sample of early-type galaxies (ETGs) from the ATLAS^{3D} HI survey by Serra et al. (2012). Similar to the RR galaxies studied here, the ETGs in ATLAS^{3D} also presented much larger HI discs than their optical sizes and the HI-richest ETGs were also found in low density environments (Serra et al. 2012). For quantitative comparison, we have attempted to match the ATLAS^{3D} sample with our SDSS galaxy catalogs. Due to the relatively low redshifts of the ATLAS^{3D} sample, none of the galaxies are included in GSWLC and only a fraction have counterparts in the NSA and the MPA/JHU catalog. Therefore, for the ATLAS^{3D} galaxies, we opt for stellar masses derived by Cappellari et al.

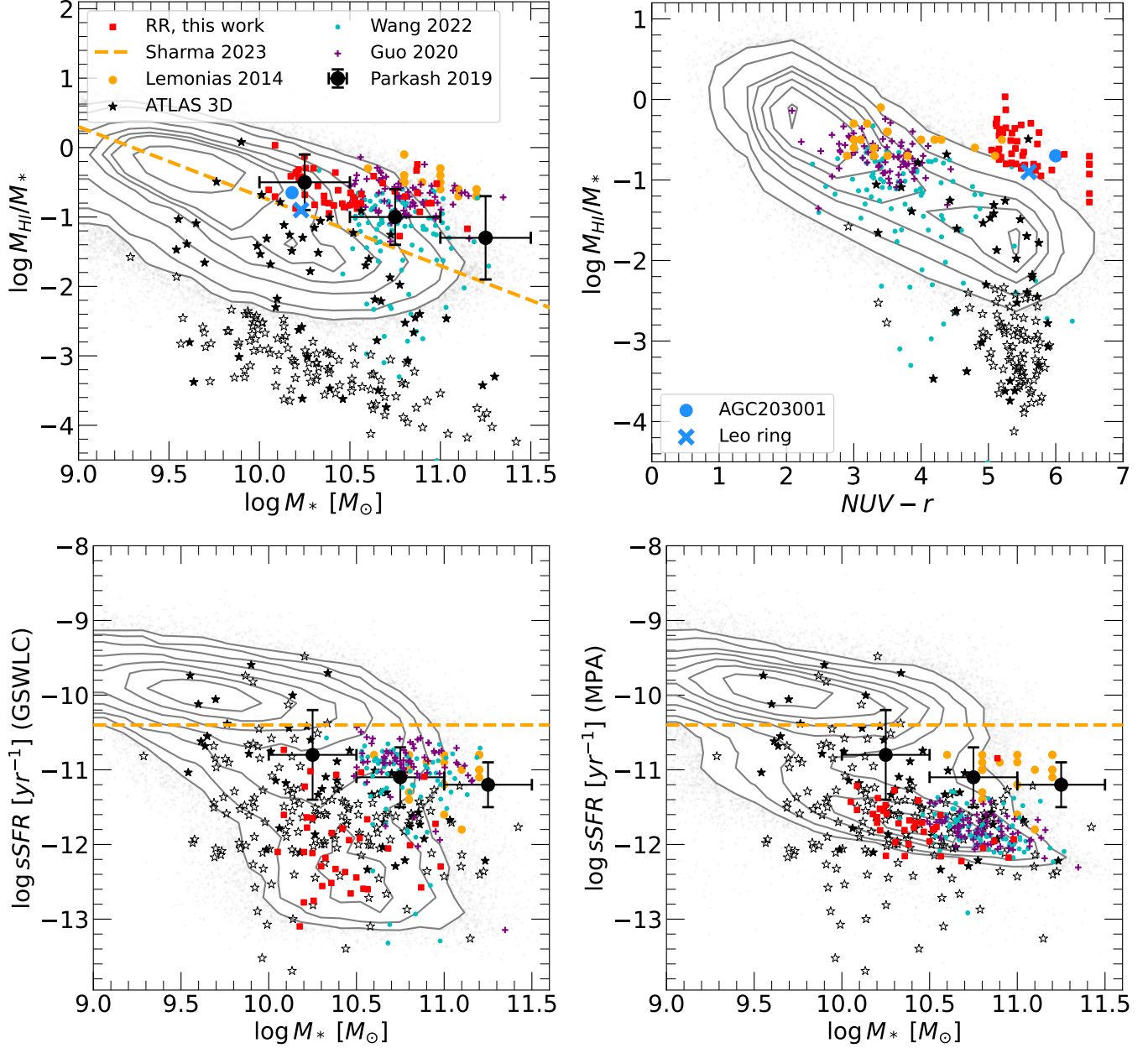


Figure 8. Comparisons of the RR sample studied in this work with previous HI samples in the diagrams of M_{HI}/M_* versus M_* (top-left), M_{HI}/M_* versus $NUV - r$ (top-right), and sSFR versus M_* (with SFRs from GSWLC in the bottom-left panel, and SFRs from the MPA/JHU catalog in the bottom-right panel). Solid and open symbols represent HI detections and non-detections (upper limits) separately. Red squares are the RR galaxies. Yellow dots are the HI-rich galaxies with suppressed star formation from [Lemonias et al. \(2014\)](#). Purple pluses and cyan dots are massive red spirals from [Guo et al. \(2020\)](#) and [Wang et al. \(2022a\)](#). Black solid dots with error bars are the median relation and scatter of the sample from [Parkash et al. \(2019\)](#). The yellow dashed lines indicate the sample selection in [Sharma et al. \(2023\)](#): $M_{\text{HI}} > 10^{9.3} M_\odot$ (top-left) and $\text{sSFR} < 10^{-10.4} \text{yr}^{-1}$ (bottom panels). Black solid and open stars represent the HI detections and non-detections (upper limits) of the ATLAS^{3D} sample, for which stellar masses are derived from M_{JAM} given by [Cappellari et al. \(2013\)](#) based on dynamical modeling and sSFRs are estimated from PAH luminosities by [Kokusho et al. \(2017\)](#) based on SED fits to data from AKARI, WISE and 2MASS. The blue cross and dot indicate the Leo ring and AGC203001 for which the HI and stellar masses and the colors are taken from [Bait et al. \(2020\)](#). The grey contours represent the SDSS volume-limited sample, of which the HI mass of each galaxy is predicted by the estimator from [Li et al. \(2022\)](#).

(2013) based on dynamical modeling, i.e. M_{JAM} in that paper. By comparing M_{JAM} with the NSA M_* for those galaxies that have counterparts in NSA, we find M_{JAM} is systematically larger by ~ 0.3 dex than M_* with no obvious dependence on M_{JAM} . To take into account this difference, we use $\log_{10} M_{\text{JAM}} - 0.3$ as the stellar mass for the ATLAS^{3D}. The SFRs are estimated by Kokusho et al. (2017) from PAH luminosities which were obtained from SED fitting to data from AKARI, WISE and 2MASS. We have compared the SFRs for those with counterparts in the MPA/JHU catalog and found no systematic differences. In Figure 8 we compare the ATLAS^{3D} sample with the RR sample in terms of the distributions of M_* , M_{HI}/M_* , $\text{NUV} - r$ and sSFR. We find that, when compared to the RR sample, the ETGs from ATLAS^{3D} mostly have similarly red colors and low sSFRs as expected, and significantly lower HI mass fractions. Only one galaxy from the ATLAS^{3D} meets our selection criteria of the RR sample, while most of them fall on or even below the contours of the general red population, indicating that the majority of red early-type galaxies are HI normal or HI poor, as generally expected. The difference between the RR sample and the general ETG population can also be seen from the bottom-right panel in Figure 3, where the RR, RN and CSC samples show very similar distributions in T-type, all dominated by early-types, but the RR sample is very different in HI mass fraction to the other two samples. The E+A galaxies previously studied are also different from our RR galaxies. In fact, Figure 3 of Zwaan et al. (2013) has shown that their E+A galaxies as well as the several from earlier studies are mostly “green” with $3 < \text{NUV} - r < 4$ and HI-normal for their color, with $\log_{10}(M_{\text{HI}}/M_*) < -1$.

The samples of HI-rich galaxies with suppressed or low star formation (Lemonias et al. 2014; Parkash et al. 2019; Sharma et al. 2023) and massive red spirals (Guo et al. 2020; Wang et al. 2022a) are more similar to our RR sample. The selection criteria of these previous samples are mentioned in section 1. The comparison of these samples with the RR sample is shown in Figure 8. As can be seen from the top-left panel, all the samples in comparison are limited to relatively high stellar mass and high HI mass fraction with respect to the complete SDSS sample, although the FAST sample from Wang et al. (2022a) includes some galaxies with low HI mass fractions. Our RR sample is distinct from other samples by having the reddest colors (top-right panel) and the lowest sSFRs (bottom-left panel), both indicating the fully quenched status of star formation in these galaxies. In contrast, both the HI-rich galaxies with suppressed star formation from Lemonias et al. (2014) and

the massive red spirals from Guo et al. (2020) and Wang et al. (2022a) are mostly “green” with intermediate colors, $3 \lesssim \text{NUV} - r \lesssim 5$, and consistently they fall mainly in the transition region between the star-forming and quiescent sequences (bottom-left panel), indicating that these galaxies are not fully quenched. As pointed out in Zhou et al. (2021), red spirals selected by optical colors such as $u - r$ are mostly green/blue in $\text{NUV} - r$, as the UV emission is more sensitive than optical colors to the ongoing weak star formation in galaxies. The fact that the sample of Parkash et al. (2019) is also limited to the transition region suggests that the criterion of mid-infrared color ($W2 - W3 < 2$) is unable to select fully quenched galaxies as well. Sharma et al. (2023) did not tabulate their galaxies, but it is natural to expect their sample to occupy similar regions in the sSFR versus M_* diagram considering the same color selection as adopted in Parkash et al. (2019). We note that massive red spirals show quite different distributions in the sSFR versus M_* diagram depending on the adopted SFR estimates. When the MPA/JHU catalog is used instead of GSWLC, these galaxies move from the transition region to the quiescent sequence, showing similarly low sSFRs to our RR galaxies. We argue that this discrepancy largely attributes to the larger uncertainties and biases in the SFRs from the MPA/JHU catalog than from the GSWLC at intermediate-to-low SFRs (see Li et al. 2023 for a recent comprehensive investigation and discussion).

We conclude that the RR sample selected in the M_{HI}/M_* versus $\text{NUV} - r$ diagram represents a unique population of galaxies, which are fully quenched but contain unusually large amounts of HI gas. Previous samples selected by $u - r$ (Guo et al. 2020; Wang et al. 2022a), or $W2 - W3$ (Parkash et al. 2019; Sharma et al. 2023), or by a fixed cut in sSFR (Lemonias et al. 2014) represent galaxies in the “green valley”, i.e. in the transition phase to being fully quenched. Their HI contents can be partly (if not fully) explained by the blue/green $\text{NUV} - r$ colors and the intermediate sSFRs.

Considering that the cessation of star formation in massive galaxies happens from inside out (e.g. Li et al. 2015; Wang et al. 2018), it could be that the HI-rich galaxies in previous samples and the RR galaxies in our sample have the same origin and follow a common evolutionary path, but they are at different stages. In this case, the RR sample and the previous samples should share some common properties. In fact, like our RR galaxies, the HI-rich galaxies in Lutz et al. (2018, 2020) were also found to have similar optical properties (e.g. the size-mass relation and radial distributions of gas metallicity) to that of HI-normal galaxies. In addi-

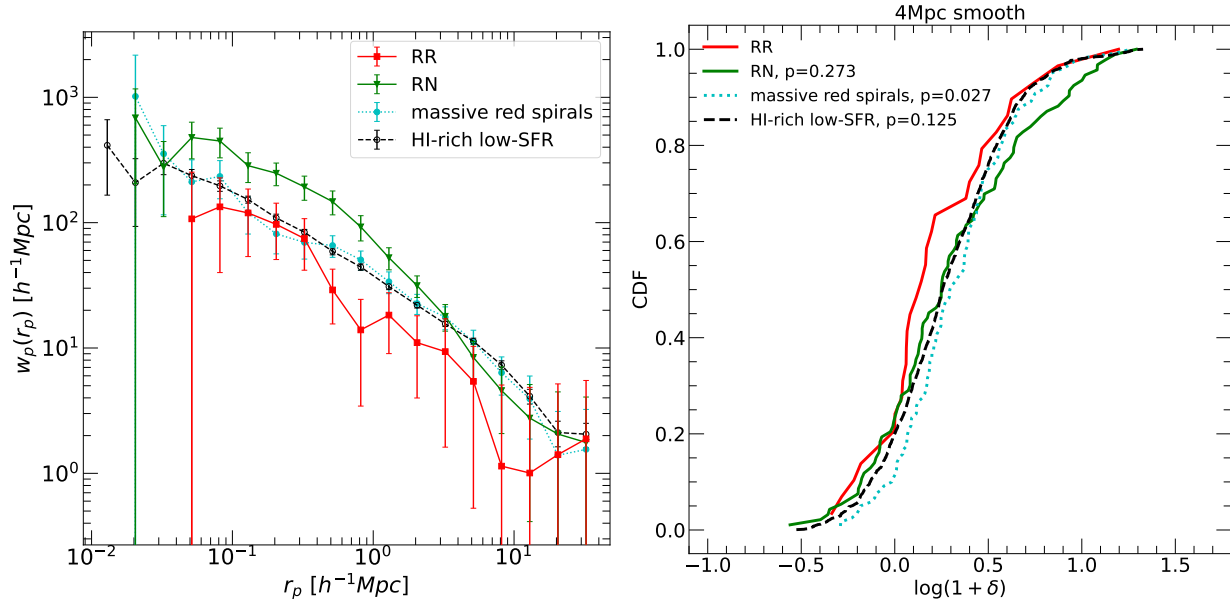


Figure 9. Projected two-point correlation function $w_p(r_p)$ (left) and cumulative distributions of local density estimated at 4 Mpc (right), as measured for the RR and RN samples studied in this work, as well as the HI-detected massive red spirals from Guo et al. (2020) and Wang et al. (2022a) and a sample selected from SDSS to mimic the HI-rich low-SFR samples studied in previous studies (see the text for details). The value of "p" in the legend of the right panel is the p-value of the two-sample KS test conducted between the RR and the corresponding sample.

tion, the large HI-to-optical size ratios found for our RR galaxies was also found in Lemonias et al. (2014) with the help of resolved HI observations: most of the massive HI-rich galaxies with suppressed star formation in their sample had HI radii at least twice as large as their optical radii (see their Figure 7). The authors found all of their galaxies had substantially low HI surface densities, likely to be the main cause of their low sSFRs. Given the even larger HI-to-optical radius ratios of our RR galaxies, they are expected to have even lower HI surface densities.

On the other hand, however, our RR galaxies also show quite different properties in many other aspects from galaxies used in previous investigations. For instance, Lemonias et al. (2014) found some evidence that AGN or bulges also contributed to the star formation suppression in their galaxies, giving support to AGN feedback and morphology quenching (Martig et al. 2009). Sharma et al. (2023) also found some evidence for AGN feedback and bar quenching for the HI-rich but low-SFR galaxies based on the IFS data from MaNGA. In addition, Parkash et al. (2019) found a high fraction (75%) of their galaxies to be LINERs or LIERs, and they speculated that the presence of HI is a precondition for LI(N)ER emission in galaxies. Sharma et al. (2023) found a similarly high fraction ($77 \pm 11\%$) of LIERs. However, they found their control sample of low-HI and low-SFR galaxies also has a high fraction

of LIERs ($60 \pm 10\%$), and concluded that HI content is not required for the high LIER fraction to correlate with the low SFR. We find no evidence for either morphology quenching, given the similar distributions in B/T and σ_* for the RR, RN and CSC samples as seen in Figure 3, or bar quenching given the similar distributions in P_{bar} as seen in Figure 4. Selected from SDSS, most of our RR galaxies do not have integral field spectroscopy, but we have examined their single-fiber SDSS spectra. We find that the emission lines relevant for AGN identification are weak in most galaxies, indicative of no AGN or LIER in their central regions. This result is consistent with the global quiescence of the RR galaxies.

In Figure 9 we compare the projected 2PCF and local densities between our RR sample and the previous samples. The samples from Lemonias et al. (2014) and Parkash et al. (2019) are too small to obtain reliable measurements, while Sharma et al. (2023) does not tabulate their galaxies. In order to compare, we select a sample of "HI-rich low-SFR" galaxies from the SDSS to mimic their samples, by applying the following two criteria: $\log_{10} M_{\text{HI}} > 9.3$ && $-11.5 < \log_{10}(\text{sSFR}) < -10.4$. We further require this sample to have the same stellar mass distribution as our RR sample. The sample includes 2,200 galaxies. The measurements for this sample are plotted as black symbols in the figure, and those of a combined sample of massive red spirals with HI detections from ALFALFA (Guo et al. 2020) and FAST

(Wang et al. 2022a) are plotted as cyan symbols. As can be seen, the “HI-rich low SFR” sample and the massive red spirals are very similar in both $w_p(r_p)$ and $\log_{10}(1+\delta)$, but when compared to them, the RR galaxies are less clustered at all scales except $r_p \sim 0.2 - 0.3 h^{-1}\text{Mpc}$ and have lower densities on average. We have also examined the central and satellite fractions of the two samples based on the SDSS group catalog, and found a central fraction of 73% for the massive red spiral galaxies and 70% for the “HI-rich low SFR” sample. These results imply that low-density environments and high central fractions are necessary conditions to make the RR galaxies a unique population, which is unlikely to entirely follow the same evolutionary pathway as the HI-rich low-SFR samples previously studied.

4.2. Existence and rareness of the RR galaxies

In a recent review, based on the xGASS sample Sain-
tonge & Catinella (2022) concluded that there is no evi-
dence for a significant population of passive galaxies
with HI reservoirs comparable to those of star-forming
main-sequence galaxies. Our result is not in contradic-
tion with theirs. As can be seen from Figure 1, xGASS
indeed contributes only a few galaxies to our RR sam-
ple. In fact, our RR sample is contributed mainly by
ALFALFA, which is much larger in sample size though
less complete in HI mass fraction when compared to
xGASS. This strongly suggests that the quenched but
HI-rich galaxies are rather rare, and they can be iden-
tified as a significant population for statistical studies
as done in this work only if the parent sample is large
enough. The rareness of the RR galaxies can be more
clearly seen when compared to the SDSS volume-limited
sample. As we have seen from Figure 2, the majority of
our RR galaxies are found beyond the 95% contour of
the SDSS sample. In addition, as can be seen in Fig-
ure 8, all the previously studied samples including the
HI-rich but low SFR sample Lemonias et al. (2014), the
massive red spirals (Guo et al. 2020; Wang et al. 2022a),
and the ATLAS^{3D} sample (Serra et al. 2012) contain a
few galaxies satisfying our criteria of RR galaxies. This
result is also consistent with both the existence and the
rareness of the RR galaxies.

Using data from both xGASS and ALFALFA, how-
ever, Zhang et al. (2019) claimed that nearly all the mas-
sive quiescent central disc galaxies are HI-rich, with M_{HI}
similar to that of star-forming galaxies. This result was
questioned by Cortese et al. (2020) who found no passive
disc galaxies in xGASS with HI reservoirs comparable to
those typical of star-forming galaxies. The authors sug-
gested that the previous claim by Zhang et al. (2019)
was due to the use of aperture-corrected SFR estimates

from the MPA/JHU catalog, in which the global star
formation of HI-rich galaxies with extended star-forming
discs is significantly underestimated. Here we revisit this
problem taking advantage of the SDSS volume-limited
sample for which we have estimated an HI mass for
each galaxy. Adopting the same sample selection as in
Zhang et al. (2019), we select a sample of 1609 mas-
sive ($10^{10.6}M_{\odot} < M_{*} < 10^{11}M_{\odot}$) central disk galaxies
using the SDSS group catalog (Yang et al. 2007) and
the SDSS morphology catalog from Domínguez Sánchez
et al. (2018). We define central galaxies as the most
massive galaxy of their group and select disk galaxies
by requiring T-type > 0 and $P_{\text{disk}} > 0.5$, where P_{disk}
is the probability for a galaxy to be a disk provided
by the morphology catalog. The average and scatter of
 M_{HI}/M_{*} and M_{HI} of this sample as functions of $\text{NUV} - r$
and SFR are plotted as the orange lines and shaded re-
gions in Figure 2. We see the massive central disc galax-
ies to roughly follow the SC and RN samples at the high-
and low-SFR ends in terms of M_{HI}/M_{*} , thus with much
lower HI mass fractions than the RR galaxies of simi-
lar SFRs. Because of their higher stellar masses, these
galaxies have higher M_{HI} than the RN and SC sam-
ples at a given $\text{NUV} - r$ or SFR, but still have lower M_{HI}
than the RR galaxies. This result suggests both that
the massive quiescent central disk galaxies investigated
in Zhang et al. (2019) are HI-poor as expected from their
red colors and low SFRs, and that these galaxies are
different from the RR galaxies in our sample which are
truly quenched, have unusually high HI mass fractions,
but are rare.

Our result is consistent with Cortese et al. (2020)
where both HI detections and non-detections from
xGASS were used to quantify the HI reservoirs of cen-
tral galaxies as a function of stellar mass, SFR and B/T .
Following the format of their Figs. 1 and 2 but using
our volume-limited SDSS sample instead of xGASS, we
examine the M_{HI} -SFR relationship for central galaxies
in different intervals of M_{*} and below different B/T up-
per limits, plotted as black contours in Figure 10 (with
SFRs from GSWLC) and Figure 11 (with SFRs from
the MPA/JHU catalog). In each panel, we indicate
the best-fitting star-forming main sequence (SFMS) and
the 2σ lower limit of the SFMS, as well as the median
HI mass of the SFMS galaxies (those falling within 1σ
around the SFMS). The low-SFR but HI-rich galaxies
are then defined to be those with SFR below the 2σ
lower limit of the SFMS and above the median M_{HI} ,
as indicated by the cyan area. We calculate the frac-
tion of the SDSS galaxies falling in this area and in-
dicate the result in each panel. As can be seen, the
fractions are small in both figures and in all panels. In

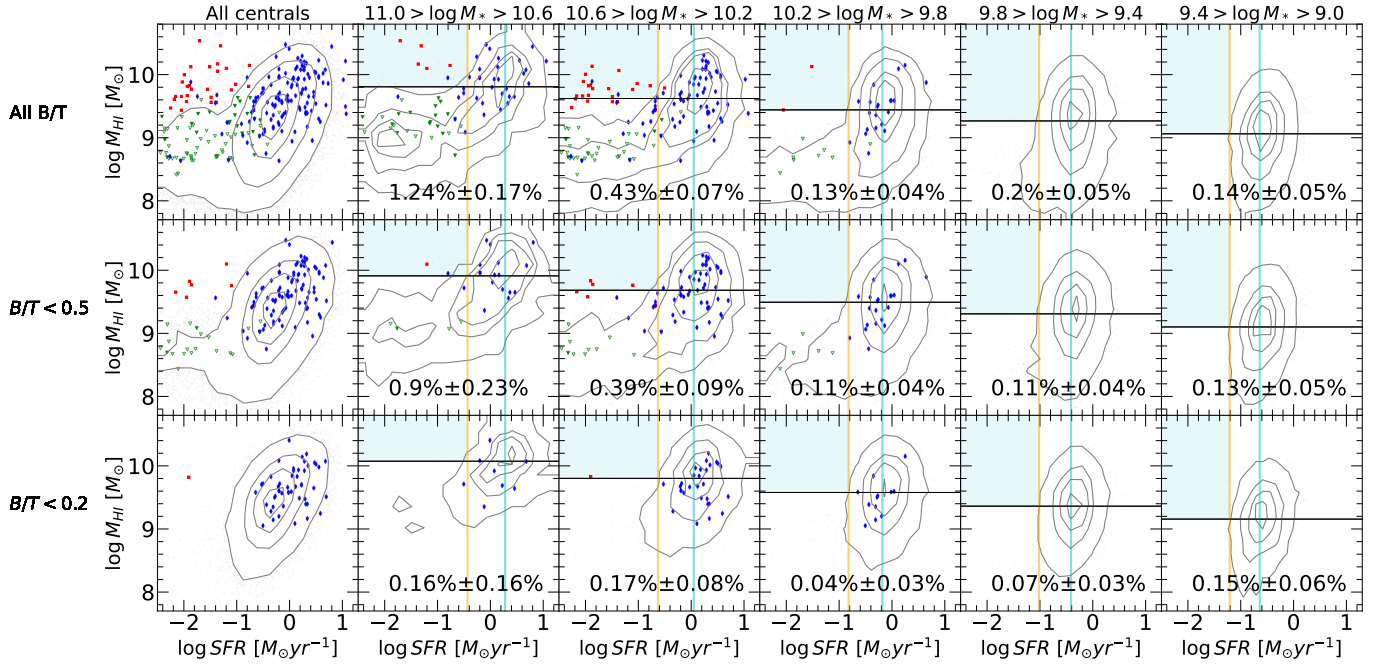


Figure 10. Distributions of central galaxies from the RR, RN, SC and SDSS samples on the M_{HI} versus SFR diagram. Panels from left to right correspond to different stellar mass ranges as indicated above the top panels, while panels from top to bottom correspond to different thresholds of the bulge-to-total ratio as indicated on the left-hand side. In each panel, the red, green and blue symbols represent the RR, RN and SC galaxies, while the black contours enclose 20%, 45%, 70% and 95% of the SDSS sample. The cyan, yellow and black lines indicate the SFR on the best-fitting star-forming main sequence (SFMS), the 2σ lower limit of the SFMS and the median HI mass of the main-sequence galaxies (those falling within 1σ around the SFMS). The fraction of HI-rich but low-SFR galaxies in the SDSS sample (i.e. those falling in the cyan region) and its Poisson error are indicated in each panel.

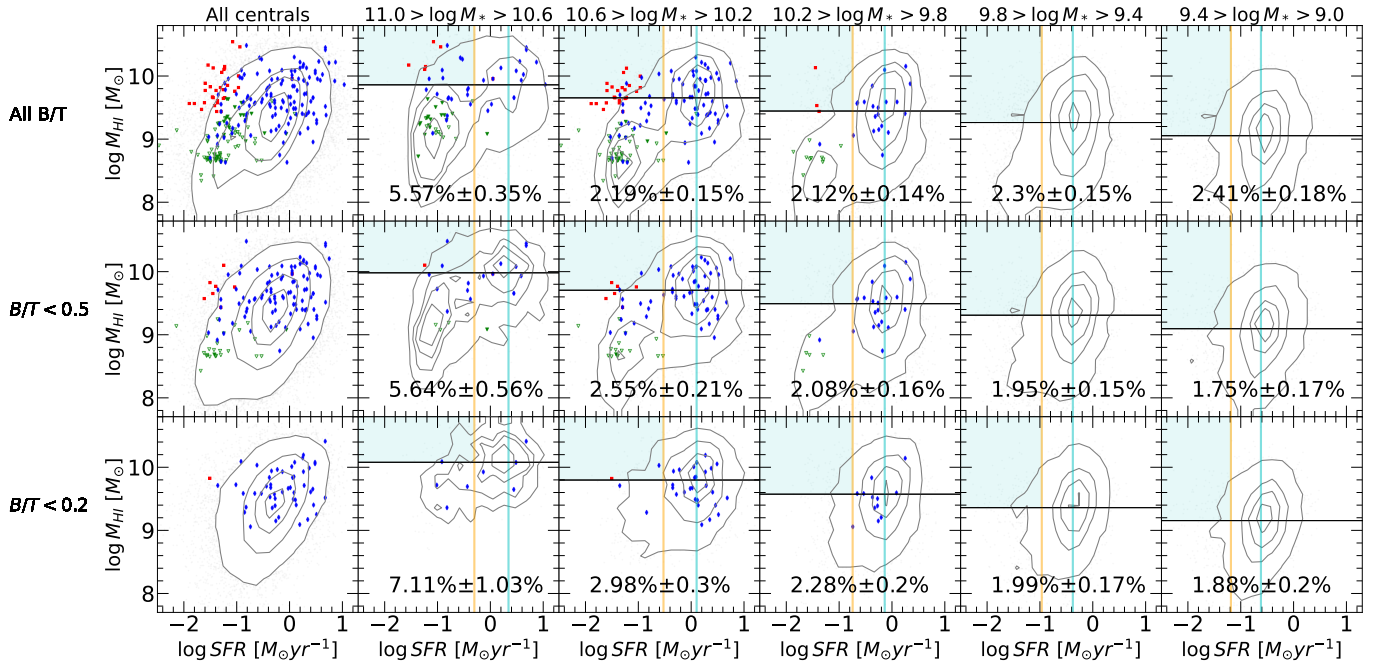


Figure 11. Same as Figure 10 except that the SFR estimates are taken from the MPA/JHU catalog instead of GSWLC.

the case with the GSWLC SFRs, the fraction is at most $(1.24 \pm 0.17)\%$ as found for all the centrals in the most massive bin, and decreases as one goes to galaxies with lower M_* and smaller B/T . Although the fractions become larger when the MPA/JHU SFRs are used, this type of galaxy is still a minor population with a fraction of $(7.11 \pm 1.03)\%$ at most. For comparison, the RR, RN and SC galaxies are plotted in both figures. Most of the RR galaxies fall in the cyan areas as expected.

We conclude that, although the quenched but HI-rich galaxies like those in our RR sample do exist in the nearby Universe, they contribute only a tiny fraction to the general population of their colors and SFRs. In other words, the majority of massive quiescent galaxies are HI-poor, as found in many previous studies (see [Saintonge & Catinella 2022](#), [Cortese et al. 2020](#), and references therein).

4.3. *Origin of the RR galaxies*

The formation scenarios of the RR galaxies are not immediately clear based on our results. The high fraction of central galaxies in the RR sample as well as the relatively low density of the local environment are both helpful for the galaxies to sustain their cold gas against environmental effects such as ram-pressure and tidal stripping, which are stronger for satellite galaxies and in denser regions. However, the origin of the large amounts of HI gas in these galaxies is still unclear. As mentioned, the large HI-to-optical size ratios of the RR galaxies imply very extended HI discs with low surface densities of HI in the outskirts. It is thus natural to expect no or weak star formation even with a substantially large amount of total HI mass. This is consistent with the finding of [Lemonias et al. \(2014\)](#) where the resolved HI observations revealed low HI densities in a sample of 20 HI-rich galaxies with suppressed SFRs. Resolved HI observations from The ATLAS^{3D} HI survey also show that about 20% of the nearby ETGs outside the Virgo Cluster are surrounded by large HI discs or rings of low column density ([Serra et al. 2012, 2014](#)), with signs of recent star formation similar to that in the outskirts of spiral galaxies ([Yıldız et al. 2015, 2017](#)). We have visually examined the optical image of our RR galaxies from the DESI Legacy Survey (see [Figure 12](#) in the [Appendix A](#)), finding about half of our galaxies to present faint and extended ring or spiral structures in the outskirts. This fraction could be even larger if deeper images are available. In addition, some of these galaxies show misalignment between the main stellar body and the extended structure, which was also observed for half of the ATLAS^{3D} ETGs that have large HI discs/rings ([Serra et al. 2012, 2014](#)). This result is consistent with the

finding of the ATLAS^{3D} survey, both supporting the external origin of the massive HI gas content, such as gas accretion and/or mergers.

The extended HI discs may be supported by high angular momentum, which is inherited from the high spin of host dark matter halos as suggested by [Lutz et al. \(2018\)](#) for their HI-extreme galaxies. [Mancera Piña et al. \(2021a\)](#) and [Mancera Piña et al. \(2021b\)](#) have recently measured the specific angular momentum for both stars and atomic gas in a sample of nearby disc galaxies, finding a strong correlation between the gas fraction and the specific angular momentum, with higher angular momenta and lower star formation efficiencies for galaxies of higher gas fractions. In particular, it was found that the HI-extreme galaxies from [Lutz et al. \(2018\)](#) tightly followed the same scaling correlations of angular momentum as galaxies of normal HI content. Although our RR galaxies differ from those previous samples in certain aspects as discussed above, they could also have high angular momentum, because of which the HI gas cannot be efficiently converted into stars. In fact, the angular momentum of circum-galactic medium (CGM) has been found to either enhance or suppress star formation in simulated disc galaxies ([Wang et al. 2022b](#); [Lu et al. 2022](#)). The ideal of “angular momentum quenching” has also been advocated in empirical models of galaxy evolution (e.g. [Obreschkow et al. 2016](#); [Peng & Renzini 2020](#)), although the model predictions are found to not fully match the current HI surveys such as xGASS ([Hardwick et al. 2022](#)). The RR galaxies studied in our work represent a unique population useful to test such models, but for this purpose one would need larger samples with both resolved HI observations and angular momentum measurements.

We should point out that, when estimating the HI sizes for our galaxies we have assumed the HI gas is distributed in a regular disk as in most HI-bearing galaxies. In fact, the only galaxy in our sample with resolved HI observations, UGC 1382 (id=0 in [Table 1](#)) indeed shows a regularly rotating HI disk. However, irregular and even off-galaxy HI distributions have been observed for a handful of HI-bearing ETGs, e.g. the giant HI ring around NGC 3384 and M 96 in the Leo group ([Schneider et al. 1983](#); [Schneider 1985, 1989](#); [Michel-Dansac et al. 2010](#)) and the large HI ring around the quiescent galaxy AGC 203001 ([Bait et al. 2020](#)). As can be seen from [Figure 8](#), both the Leo ring and AGC 203001 meet the selection criteria of our RR sample. Therefore, it is possible that some fraction of our RR galaxies also show similarly irregular HI distributions. Although its physical origin is still under debate, such HI-dominated rings are likely expelled gas from HI-rich ETGs caused

by a collision with an intruder galaxy (Michel-Dansac et al. 2010; Bait et al. 2020, e.g.) or tidal tripping by the group potential (e.g. Bekki et al. 2005; Serra et al. 2013; Corbelli et al. 2021), or falling back of the tidal tail of gas-rich major mergers (e.g. Morganti et al. 2003; Sameer et al. 2022). Considering the extreme paucity of such observational cases in the literature as well as the fact that the majority of our RR galaxies have no close companions, we would expect such an irregular or off-galaxy HI distribution to be not a common feature in the RR galaxies. Resolved HI observations for the RR galaxies would be necessary in order to test out this conjecture.

5. SUMMARY

In this work we have identified and investigated a rare population of *red but HI-rich* (RR) galaxies in the local Universe. We make use of three HI surveys including ALFALFA, xGASS and HI-MaNGA, from which we select a sample of 47 RR galaxies on the diagram of $\log_{10}(M_{\text{HI}}/M_*)$ versus $\text{NUV} - r$. Our RR galaxies are required to have $\text{NUV} - r > 5$, and be outliers in the distribution of $\log_{10}(M_{\text{HI}}/M_*)$, located outside the 95% contour of a volume-limited sample of SDSS for which we have estimated an HI mass for each galaxy based on Bayesian inferences of its optical properties. The RR galaxies are relatively massive, with stellar mass $M_* \gtrsim 10^{10} M_\odot$. For comparison we have selected a control sample of “red and HI-normal” (RN) galaxies that are closely matched with the RR sample in M_* and $\text{NUV} - r$, as well as a “stellar mass control” (SC) sample that is matched only in M_* . We have demonstrated that the RN sample is representative to the massive red galaxy population (Figure 3 and Figure 6).

We have examined a variety of optical properties, finding the RR and RN samples to be very similar in all the properties, which are typical of massive red (quenched) galaxies in the SDSS volume-limited sample. We have also examined the environment of our samples, as quantified by three different statistics: overdensity of the local environment ($1 + \delta$) as estimated at 2 Mpc and 4 Mpc, projected two-point cross-correlation function $w_p(r_p)$ with respect to a reference sample of half a million galaxies from the SDSS spectroscopic survey, and background-subtracted neighbor counts $N_c(< R_p)$ estimated with the SDSS photometric sample down to r -band magnitude of $r_{\text{lim}} = 21$ mag. We find the RR sample to be associated with lower density environments at a scale of 4 Mpc, and have lower clustering amplitudes and smaller neighbor counts at intermediate scales from a few $\times 100$ kpc to a few Mpc, when compared to the RN sample. These results imply that the RR galax-

ies are preferentially located at the center of relatively low-mass dark matter halos. This is confirmed by the SDSS galaxy group catalog which reveals that about 89% of our RR galaxies are indeed the central galaxy of their groups, compared to a central fraction of $\sim 60\%$ for the RN sample. The median halo mass of the RR sample is found to be $M_h \sim 10^{12} h^{-1} M_\odot$, compared to $M_h \sim 10^{12.5} h^{-1} M_\odot$ for the RN sample. Furthermore, we have estimated the HI disk size for each of our galaxies based on the tight HI size-mass relation from the literature. We find an average HI-to-optical size ratio of $R_{\text{HI}}/R_{90} \sim 4$ for the RR sample, which is four times the average ratio found for the RN sample.

We have compared our RR sample with similar samples investigated in previous studies. We find the previous samples are dominated by star-forming galaxies with extremely-high HI content, or quenched HI-poor galaxies, or transition galaxies with blue-to-green colors and intermediate SFRs, thus falling in between the star-forming main sequence and the quiescent sequence. Our RR galaxies are unique for their (NUV-to-optical) red colors indicative of fully-quenched star formation status and simultaneously high fractions of HI mass. We use the SDSS volume-limited sample with estimated HI masses to show that, although the RR galaxies form a unique population, they are rather rare, contributing only a tiny fraction of the quenched galaxy population. The majority of massive quenched galaxies in the low-redshift Universe are HI-poor.

ACKNOWLEDGMENTS

We are grateful to the anonymous referee for the helpful comments. This work is supported by the National Key R&D Program of China (grant NO. 2022YFA1602902), and the National Natural Science Foundation of China (grant Nos. 11821303, 11733002, 11973030, 11673015, 11733004, 11761131004, 11761141012). This work has made use of the following softwares: Numpy (Harris et al. 2020), Matplotlib (Hunter 2007), Astropy (Astropy Collaboration et al. 2013, 2018, 2022), Scipy (Virtanen et al. 2020), corner (Foreman-Mackey 2016), and Seaborn (Waskom 2021).

Funding for the SDSS and SDSS-II has been provided by the Alfred P. Sloan Foundation, the Participating Institutions, the National Science Foundation, the U.S. Department of Energy, the National Aeronautics and Space Administration, the Japanese Monbukagakusho, the Max Planck Society, and the Higher Education Funding Council for England. The SDSS Web Site is <http://www.sdss.org/>.

The SDSS is managed by the Astrophysical Research Consortium for the Participating Institutions. The Par-

ticipating Institutions are the American Museum of Natural History, Astrophysical Institute Potsdam, University of Basel, University of Cambridge, Case Western Reserve University, University of Chicago, Drexel University, Fermilab, the Institute for Advanced Study, the Japan Participation Group, Johns Hopkins University, the Joint Institute for Nuclear Astrophysics, the Kavli Institute for Particle Astrophysics and Cosmology, the

Korean Scientist Group, the Chinese Academy of Sciences (LAMOST), Los Alamos National Laboratory, the Max-Planck-Institute for Astronomy (MPIA), the Max-Planck-Institute for Astrophysics (MPA), New Mexico State University, Ohio State University, University of Pittsburgh, University of Portsmouth, Princeton University, the United States Naval Observatory, and the University of Washington.

REFERENCES

- Adelman-McCarthy, J. K., Agüeros, M. A., Allam, S. S., et al. 2008, *The Astrophysical Journal Supplement Series*, 175, 297, doi: [10.1086/524984](https://doi.org/10.1086/524984)
- Astropy Collaboration, Robitaille, T. P., Tollerud, E. J., et al. 2013, *A&A*, 558, A33, doi: [10.1051/0004-6361/201322068](https://doi.org/10.1051/0004-6361/201322068)
- Astropy Collaboration, Price-Whelan, A. M., Sipőcz, B. M., et al. 2018, *AJ*, 156, 123, doi: [10.3847/1538-3881/aabc4f](https://doi.org/10.3847/1538-3881/aabc4f)
- Astropy Collaboration, Price-Whelan, A. M., Lim, P. L., et al. 2022, *ApJ*, 935, 167, doi: [10.3847/1538-4357/ac7c74](https://doi.org/10.3847/1538-4357/ac7c74)
- Bait, O., Kurapati, S., Duc, P.-A., et al. 2020, *MNRAS*, 492, 1, doi: [10.1093/mnras/stz2972](https://doi.org/10.1093/mnras/stz2972)
- Balogh, M. L., Morris, S. L., Yee, H. K. C., Carlberg, R. G., & Ellingson, E. 1999, *ApJ*, 527, 54, doi: [10.1086/308056](https://doi.org/10.1086/308056)
- Bekki, K., Koribalski, B. S., Ryder, S. D., & Couch, W. J. 2005, *MNRAS*, 357, L21, doi: [10.1111/j.1745-3933.2005.08625.x](https://doi.org/10.1111/j.1745-3933.2005.08625.x)
- Blanton, M. R., Kazin, E., Muna, D., Weaver, B. A., & Price-Whelan, A. 2011, *AJ*, 142, 31, doi: [10.1088/0004-6256/142/1/31](https://doi.org/10.1088/0004-6256/142/1/31)
- Blanton, M. R., & Roweis, S. 2007, *AJ*, 133, 734, doi: [10.1086/510127](https://doi.org/10.1086/510127)
- Blanton, M. R., Schlegel, D. J., Strauss, M. A., et al. 2005, *The Astronomical Journal*, 129, 2562, doi: [10.1086/429803](https://doi.org/10.1086/429803)
- Bregman, J. N., Hogg, D. E., & Roberts, M. S. 1992, *ApJ*, 387, 484, doi: [10.1086/171101](https://doi.org/10.1086/171101)
- Brinchmann, J., Charlot, S., White, S. D. M., et al. 2004, *MNRAS*, 351, 1151, doi: [10.1111/j.1365-2966.2004.07881.x](https://doi.org/10.1111/j.1365-2966.2004.07881.x)
- Brown, T., Catinella, B., Cortese, L., et al. 2015, *MNRAS*, 452, 2479, doi: [10.1093/mnras/stv1311](https://doi.org/10.1093/mnras/stv1311)
- Bruzual, G., & Charlot, S. 2003, *MNRAS*, 344, 1000, doi: [10.1046/j.1365-8711.2003.06897.x](https://doi.org/10.1046/j.1365-8711.2003.06897.x)
- Bundy, K., Bershady, M. A., Law, D. R., et al. 2014, *The Astrophysical Journal*, 798, 7, doi: [10.1088/0004-637X/798/1/7](https://doi.org/10.1088/0004-637X/798/1/7)
- Buyle, P., De Rijcke, S., & Dejonghe, H. 2008, *ApJL*, 684, L17, doi: [10.1086/591316](https://doi.org/10.1086/591316)
- Buyle, P., Michielsen, D., De Rijcke, S., et al. 2006, *ApJ*, 649, 163, doi: [10.1086/505633](https://doi.org/10.1086/505633)
- Cappellari, M., Emsellem, E., Krajnović, D., et al. 2011, *MNRAS*, 413, 813, doi: [10.1111/j.1365-2966.2010.18174.x](https://doi.org/10.1111/j.1365-2966.2010.18174.x)
- Cappellari, M., Scott, N., Alatalo, K., et al. 2013, *MNRAS*, 432, 1709, doi: [10.1093/mnras/stt562](https://doi.org/10.1093/mnras/stt562)
- Catinella, B., Schiminovich, D., Kauffmann, G., et al. 2010, *MNRAS*, 403, 683, doi: [10.1111/j.1365-2966.2009.16180.x](https://doi.org/10.1111/j.1365-2966.2009.16180.x)
- Catinella, B., Saintonge, A., Janowiecki, S., et al. 2018, *Monthly Notices of the Royal Astronomical Society*, 476, 875, doi: [10.1093/mnras/sty089](https://doi.org/10.1093/mnras/sty089)
- Chabrier, G. 2003, *PASP*, 115, 763, doi: [10.1086/376392](https://doi.org/10.1086/376392)
- Chang, T.-C., van Gorkom, J. H., Zabludoff, A. I., Zaritsky, D., & Mihos, J. C. 2001, *AJ*, 121, 1965, doi: [10.1086/319959](https://doi.org/10.1086/319959)
- Colless, M., Dalton, G., Maddox, S., et al. 2001, *MNRAS*, 328, 1039, doi: [10.1046/j.1365-8711.2001.04902.x](https://doi.org/10.1046/j.1365-8711.2001.04902.x)
- Corbelli, E., Cresci, G., Mannucci, F., Thilker, D., & Venturi, G. 2021, *ApJL*, 908, L39, doi: [10.3847/2041-8213/abdf64](https://doi.org/10.3847/2041-8213/abdf64)
- Cortese, L., Catinella, B., Cook, R. H. W., & Janowiecki, S. 2020, *MNRAS*, 494, L42, doi: [10.1093/mnrasl/slaa032](https://doi.org/10.1093/mnrasl/slaa032)
- di Serego Alighieri, S., Gavazzi, G., Giovanardi, C., et al. 2007, *A&A*, 474, 851, doi: [10.1051/0004-6361:20078205](https://doi.org/10.1051/0004-6361:20078205)
- Domínguez Sánchez, H., Huertas-Company, M., Bernardi, M., Tuccillo, D., & Fischer, J. L. 2018, *MNRAS*, 476, 3661, doi: [10.1093/mnras/sty338](https://doi.org/10.1093/mnras/sty338)
- Foreman-Mackey, D. 2016, *The Journal of Open Source Software*, 1, 24, doi: [10.21105/joss.00024](https://doi.org/10.21105/joss.00024)
- Geréb, K., Catinella, B., Cortese, L., et al. 2016, *MNRAS*, 462, 382, doi: [10.1093/mnras/stw1675](https://doi.org/10.1093/mnras/stw1675)
- Geréb, K., Janowiecki, S., Catinella, B., Cortese, L., & Kilborn, V. 2018, *MNRAS*, 476, 896, doi: [10.1093/mnras/sty214](https://doi.org/10.1093/mnras/sty214)
- Giovanelli, R., Haynes, M. P., Kent, B. R., et al. 2005, *The Astronomical Journal*, 130, 2598, doi: [10.1086/497431](https://doi.org/10.1086/497431)
- Grossi, M., di Serego Alighieri, S., Giovanardi, C., et al. 2009, *A&A*, 498, 407, doi: [10.1051/0004-6361/200810823](https://doi.org/10.1051/0004-6361/200810823)

- Guo, R., Hao, C.-N., Xia, X., et al. 2020, *ApJ*, 897, 162, doi: [10.3847/1538-4357/ab9b75](https://doi.org/10.3847/1538-4357/ab9b75)
- Hagen, L. M. Z., Seibert, M., Hagen, A., et al. 2016, *ApJ*, 826, 210, doi: [10.3847/0004-637X/826/2/210](https://doi.org/10.3847/0004-637X/826/2/210)
- Hardwick, J. A., Cortese, L., Obreschkow, D., & Catinella, B. 2022, *MNRAS*, 516, 4043, doi: [10.1093/mnras/stac2476](https://doi.org/10.1093/mnras/stac2476)
- Harris, C. R., Millman, K. J., van der Walt, S. J., et al. 2020, *Nature*, 585, 357, doi: [10.1038/s41586-020-2649-2](https://doi.org/10.1038/s41586-020-2649-2)
- Haynes, M. P., & Giovanelli, R. 1984, *AJ*, 89, 758, doi: [10.1086/113573](https://doi.org/10.1086/113573)
- Haynes, M. P., Giovanelli, R., Kent, B. R., et al. 2018, *ApJ*, 861, 49, doi: [10.3847/1538-4357/aac956](https://doi.org/10.3847/1538-4357/aac956)
- Huang, S., Haynes, M. P., Giovanelli, R., & Brinchmann, J. 2012, *ApJ*, 756, 113, doi: [10.1088/0004-637X/756/2/113](https://doi.org/10.1088/0004-637X/756/2/113)
- Huang, S., Haynes, M. P., Giovanelli, R., et al. 2014, *ApJ*, 793, 40, doi: [10.1088/0004-637X/793/1/40](https://doi.org/10.1088/0004-637X/793/1/40)
- Hunter, J. D. 2007, *Computing in Science and Engineering*, 9, 90, doi: [10.1109/MCSE.2007.55](https://doi.org/10.1109/MCSE.2007.55)
- Jiang, P., Tang, N.-Y., Hou, L.-G., et al. 2020, *Research in Astronomy and Astrophysics*, 20, 064, doi: [10.1088/1674-4527/20/5/64](https://doi.org/10.1088/1674-4527/20/5/64)
- Kannappan, S. J. 2004, *ApJL*, 611, L89, doi: [10.1086/423785](https://doi.org/10.1086/423785)
- Kennicutt, Robert C., J. 1998, *ApJ*, 498, 541, doi: [10.1086/305588](https://doi.org/10.1086/305588)
- Knapp, G. R., Turner, E. L., & Cunniffe, P. E. 1985, *AJ*, 90, 454, doi: [10.1086/113751](https://doi.org/10.1086/113751)
- Kokusho, T., Kaneda, H., Bureau, M., et al. 2017, *A&A*, 605, A74, doi: [10.1051/0004-6361/201630158](https://doi.org/10.1051/0004-6361/201630158)
- Lee, C., Chung, A., Yun, M. S., et al. 2014, *MNRAS*, 441, 1363, doi: [10.1093/mnras/stu670](https://doi.org/10.1093/mnras/stu670)
- Lemonias, J. J., Schiminovich, D., Catinella, B., Heckman, T. M., & Moran, S. M. 2014, *ApJ*, 790, 27, doi: [10.1088/0004-637X/790/1/27](https://doi.org/10.1088/0004-637X/790/1/27)
- Li, C., Kauffmann, G., Fu, J., et al. 2012, *MNRAS*, 424, 1471, doi: [10.1111/j.1365-2966.2012.21337.x](https://doi.org/10.1111/j.1365-2966.2012.21337.x)
- Li, C., Kauffmann, G., Heckman, T. M., Jing, Y. P., & White, S. D. M. 2008a, *MNRAS*, 385, 1903, doi: [10.1111/j.1365-2966.2008.13000.x](https://doi.org/10.1111/j.1365-2966.2008.13000.x)
- Li, C., Kauffmann, G., Heckman, T. M., White, S. D. M., & Jing, Y. P. 2008b, *MNRAS*, 385, 1915, doi: [10.1111/j.1365-2966.2008.13023.x](https://doi.org/10.1111/j.1365-2966.2008.13023.x)
- Li, C., Kauffmann, G., Jing, Y. P., et al. 2006a, *MNRAS*, 368, 21, doi: [10.1111/j.1365-2966.2006.10066.x](https://doi.org/10.1111/j.1365-2966.2006.10066.x)
- Li, C., Kauffmann, G., Wang, L., et al. 2006b, *MNRAS*, 373, 457, doi: [10.1111/j.1365-2966.2006.11079.x](https://doi.org/10.1111/j.1365-2966.2006.11079.x)
- Li, C., Wang, E., Lin, L., et al. 2015, *ApJ*, 804, 125, doi: [10.1088/0004-637X/804/2/125](https://doi.org/10.1088/0004-637X/804/2/125)
- Li, X., Li, C., Mo, H. J., Xiao, T., & Wang, J. 2022, *ApJ*, 941, 48, doi: [10.3847/1538-4357/ac9ccb](https://doi.org/10.3847/1538-4357/ac9ccb)
- Li, Y. A., Ho, L. C., Shangguan, J., Zhuang, M.-Y., & Li, R. 2023, *ApJS*, 267, 17, doi: [10.3847/1538-4365/acd4b5](https://doi.org/10.3847/1538-4365/acd4b5)
- Liu, S., Luo, A. L., Zhang, W., et al. 2023, *Research in Astronomy and Astrophysics*, 23, 065006, doi: [10.1088/1674-4527/accb78](https://doi.org/10.1088/1674-4527/accb78)
- Lu, S., Xu, D., Wang, S., et al. 2022, *MNRAS*, 509, 2707, doi: [10.1093/mnras/stab3169](https://doi.org/10.1093/mnras/stab3169)
- Lutz, K. A., Kilborn, V., Catinella, B., et al. 2020, *A&A*, 635, A69, doi: [10.1051/0004-6361/201936556](https://doi.org/10.1051/0004-6361/201936556)
- Lutz, K. A., Kilborn, V. A., Catinella, B., et al. 2017, *MNRAS*, 467, 1083, doi: [10.1093/mnras/stx053](https://doi.org/10.1093/mnras/stx053)
- Lutz, K. A., Kilborn, V. A., Koribalski, B. S., et al. 2018, *MNRAS*, 476, 3744, doi: [10.1093/mnras/sty387](https://doi.org/10.1093/mnras/sty387)
- Mancera Piña, P. E., Posti, L., Fraternali, F., Adams, E. A. K., & Oosterloo, T. 2021a, *A&A*, 647, A76, doi: [10.1051/0004-6361/202039340](https://doi.org/10.1051/0004-6361/202039340)
- Mancera Piña, P. E., Posti, L., Pezzulli, G., et al. 2021b, *A&A*, 651, L15, doi: [10.1051/0004-6361/202141574](https://doi.org/10.1051/0004-6361/202141574)
- Martig, M., Bournaud, F., Teyssier, R., & Dekel, A. 2009, *ApJ*, 707, 250, doi: [10.1088/0004-637X/707/1/250](https://doi.org/10.1088/0004-637X/707/1/250)
- Martin, D. C., Fanson, J., Schiminovich, D., et al. 2005, *The Astrophysical Journal*, 619, L1, doi: [10.1086/426387](https://doi.org/10.1086/426387)
- Meert, A., Vikram, V., & Bernardi, M. 2015, *mnras*, 446, 3943, doi: [10.1093/mnras/stu2333](https://doi.org/10.1093/mnras/stu2333)
- Meyer, M. J., Zwaan, M. A., Webster, R. L., et al. 2004, *MNRAS*, 350, 1195, doi: [10.1111/j.1365-2966.2004.07710.x](https://doi.org/10.1111/j.1365-2966.2004.07710.x)
- Michel-Dansac, L., Duc, P.-A., Bournaud, F., et al. 2010, *ApJL*, 717, L143, doi: [10.1088/2041-8205/717/2/L143](https://doi.org/10.1088/2041-8205/717/2/L143)
- Mo, H., van den Bosch, F. C., & White, S. 2010, *Galaxy Formation and Evolution*
- Morganti, R., Oosterloo, T. A., Capetti, A., et al. 2003, *A&A*, 399, 511, doi: [10.1051/0004-6361:20021806](https://doi.org/10.1051/0004-6361:20021806)
- Morganti, R., de Zeeuw, P. T., Oosterloo, T. A., et al. 2006, *MNRAS*, 371, 157, doi: [10.1111/j.1365-2966.2006.10681.x](https://doi.org/10.1111/j.1365-2966.2006.10681.x)
- Nair, P. B., & Abraham, R. G. 2010, *apjs*, 186, 427, doi: [10.1088/0067-0049/186/2/427](https://doi.org/10.1088/0067-0049/186/2/427)
- Nan, R. 2006, *Science in China: Physics, Mechanics and Astronomy*, 49, 129, doi: [10.1007/s11433-006-0129-9](https://doi.org/10.1007/s11433-006-0129-9)
- Obreschkow, D., Glazebrook, K., Kilborn, V., & Lutz, K. 2016, *ApJL*, 824, L26, doi: [10.3847/2041-8205/824/2/L26](https://doi.org/10.3847/2041-8205/824/2/L26)
- Parkash, V., Brown, M. J. I., Jarrett, T. H., Fraser-McKelvie, A., & Cluver, M. E. 2019, *MNRAS*, 485, 3169, doi: [10.1093/mnras/stz593](https://doi.org/10.1093/mnras/stz593)
- Peebles, P. J. E. 2022, *Annals of Physics*, 447, 169159, doi: [10.1016/j.aop.2022.169159](https://doi.org/10.1016/j.aop.2022.169159)
- Peng, Y.-j., & Renzini, A. 2020, *MNRAS*, 491, L51, doi: [10.1093/mnras/slz163](https://doi.org/10.1093/mnras/slz163)

- Pracy, M. B., Owers, M. S., Zwaan, M., et al. 2014, MNRAS, 443, 388, doi: [10.1093/mnras/stu1103](https://doi.org/10.1093/mnras/stu1103)
- Randriamampandry, T. H., Wang, J., & Mogotsi, K. M. 2021, ApJ, 916, 26, doi: [10.3847/1538-4357/ac0442](https://doi.org/10.3847/1538-4357/ac0442)
- Saintonge, A., & Catinella, B. 2022, ARA&A, 60, 319, doi: [10.1146/annurev-astro-021022-043545](https://doi.org/10.1146/annurev-astro-021022-043545)
- Salim, S., Boquien, M., & Lee, J. C. 2018, ApJ, 859, 11, doi: [10.3847/1538-4357/aabf3c](https://doi.org/10.3847/1538-4357/aabf3c)
- Sameer, Charlton, J. C., Kacprzak, G. G., et al. 2022, MNRAS, 510, 5796, doi: [10.1093/mnras/stac052](https://doi.org/10.1093/mnras/stac052)
- Schneider, S. 1985, ApJL, 288, L33, doi: [10.1086/184416](https://doi.org/10.1086/184416)
- Schneider, S. E. 1989, ApJ, 343, 94, doi: [10.1086/167687](https://doi.org/10.1086/167687)
- Schneider, S. E., Helou, G., Salpeter, E. E., & Terzian, Y. 1983, ApJL, 273, L1, doi: [10.1086/184118](https://doi.org/10.1086/184118)
- Serra, P., Oosterloo, T., Morganti, R., et al. 2012, MNRAS, 422, 1835, doi: [10.1111/j.1365-2966.2012.20219.x](https://doi.org/10.1111/j.1365-2966.2012.20219.x)
- Serra, P., Koribalski, B., Duc, P.-A., et al. 2013, MNRAS, 428, 370, doi: [10.1093/mnras/sts033](https://doi.org/10.1093/mnras/sts033)
- Serra, P., Oser, L., Krajnóvić, D., et al. 2014, MNRAS, 444, 3388, doi: [10.1093/mnras/stt2496](https://doi.org/10.1093/mnras/stt2496)
- Sharma, A., Masters, K. L., Stark, D. V., et al. 2023, MNRAS, doi: [10.1093/mnras/stad2695](https://doi.org/10.1093/mnras/stad2695)
- Stark, D. V., Masters, K. L., Avila-Reese, V., et al. 2021, MNRAS, 503, 1345, doi: [10.1093/mnras/stab566](https://doi.org/10.1093/mnras/stab566)
- Virtanen, P., Gommers, R., Oliphant, T. E., et al. 2020, Nature Methods, 17, 261, doi: [10.1038/s41592-019-0686-2](https://doi.org/10.1038/s41592-019-0686-2)
- Wang, E., Wang, J., Kauffmann, G., Józsa, G. I. G., & Li, C. 2015, MNRAS, 449, 2010, doi: [10.1093/mnras/stv390](https://doi.org/10.1093/mnras/stv390)
- Wang, E., Li, C., Xiao, T., et al. 2018, ApJ, 856, 137, doi: [10.3847/1538-4357/aab263](https://doi.org/10.3847/1538-4357/aab263)
- Wang, H., Mo, H. J., Yang, X., et al. 2016a, ApJ, 831, 164, doi: [10.3847/0004-637X/831/2/164](https://doi.org/10.3847/0004-637X/831/2/164)
- Wang, J., Koribalski, B. S., Serra, P., et al. 2016b, MNRAS, 460, 2143, doi: [10.1093/mnras/stw1099](https://doi.org/10.1093/mnras/stw1099)
- Wang, J., Kauffmann, G., Józsa, G. I. G., et al. 2013, MNRAS, 433, 270, doi: [10.1093/mnras/stt722](https://doi.org/10.1093/mnras/stt722)
- Wang, L., & Li, C. 2019, MNRAS, 483, 1452, doi: [10.1093/mnras/sty3204](https://doi.org/10.1093/mnras/sty3204)
- Wang, L., Zheng, Z., Hao, C.-N., et al. 2022a, MNRAS, 516, 2337, doi: [10.1093/mnras/stac2292](https://doi.org/10.1093/mnras/stac2292)
- Wang, S., Xu, D., Lu, S., et al. 2022b, MNRAS, 509, 3148, doi: [10.1093/mnras/stab3167](https://doi.org/10.1093/mnras/stab3167)
- Wardle, M., & Knapp, G. R. 1986, AJ, 91, 23, doi: [10.1086/113976](https://doi.org/10.1086/113976)
- Waskom, M. L. 2021, Journal of Open Source Software, 6, 3021, doi: [10.21105/joss.03021](https://doi.org/10.21105/joss.03021)
- White, S. D. M., & Rees, M. J. 1978, MNRAS, 183, 341, doi: [10.1093/mnras/183.3.341](https://doi.org/10.1093/mnras/183.3.341)
- Willett, K. W., Lintott, C. J., Bamford, S. P., et al. 2013, MNRAS, 435, 2835, doi: [10.1093/mnras/stt1458](https://doi.org/10.1093/mnras/stt1458)
- Yang, X., Mo, H. J., van den Bosch, F. C., et al. 2007, ApJ, 671, 153, doi: [10.1086/522027](https://doi.org/10.1086/522027)
- Yıldız, M. K., Serra, P., Oosterloo, T. A., et al. 2015, MNRAS, 451, 103, doi: [10.1093/mnras/stv992](https://doi.org/10.1093/mnras/stv992)
- Yıldız, M. K., Serra, P., Peletier, R. F., Oosterloo, T. A., & Duc, P.-A. 2017, MNRAS, 464, 329, doi: [10.1093/mnras/stw2294](https://doi.org/10.1093/mnras/stw2294)
- York, D. G., Adelman, J., Anderson, John E., J., et al. 2000, AJ, 120, 1579, doi: [10.1086/301513](https://doi.org/10.1086/301513)
- Young, L. M., Scott, N., Serra, P., et al. 2014, MNRAS, 444, 3408, doi: [10.1093/mnras/stt2474](https://doi.org/10.1093/mnras/stt2474)
- Zasov, A. V., & Zaitseva, N. A. 2022, Astronomy Reports, 66, 755, doi: [10.1134/S1063772922090128](https://doi.org/10.1134/S1063772922090128)
- Zhang, C., Peng, Y., Ho, L. C., et al. 2019, ApJL, 884, L52, doi: [10.3847/2041-8213/ab4ae4](https://doi.org/10.3847/2041-8213/ab4ae4)
- Zhang, W., Li, C., Kauffmann, G., et al. 2009, MNRAS, 397, 1243, doi: [10.1111/j.1365-2966.2009.15050.x](https://doi.org/10.1111/j.1365-2966.2009.15050.x)
- Zhou, S., Li, C., Hao, C.-N., et al. 2021, ApJ, 916, 38, doi: [10.3847/1538-4357/ac06cc](https://doi.org/10.3847/1538-4357/ac06cc)
- Zwaan, M. A., Kuntschner, H., Pracy, M. B., & Couch, W. J. 2013, MNRAS, 432, 492, doi: [10.1093/mnras/stt496](https://doi.org/10.1093/mnras/stt496)

APPENDIX

A. THE OPTICAL IMAGES OF THE RR SAMPLE

Figure 12 displays the optical images of the RR sample. The image of galaxy 39 is taken from the SDSS DR16 Skyserver⁴, and the images of the other galaxies are taken from the DESI Legacy Survey⁵. The images are ordered by decreasing HI-to-stellar mass ratio from top left to bottom right. The ID and HI-to-stellar mass ratio of each galaxy are indicated on top of the corresponding image.

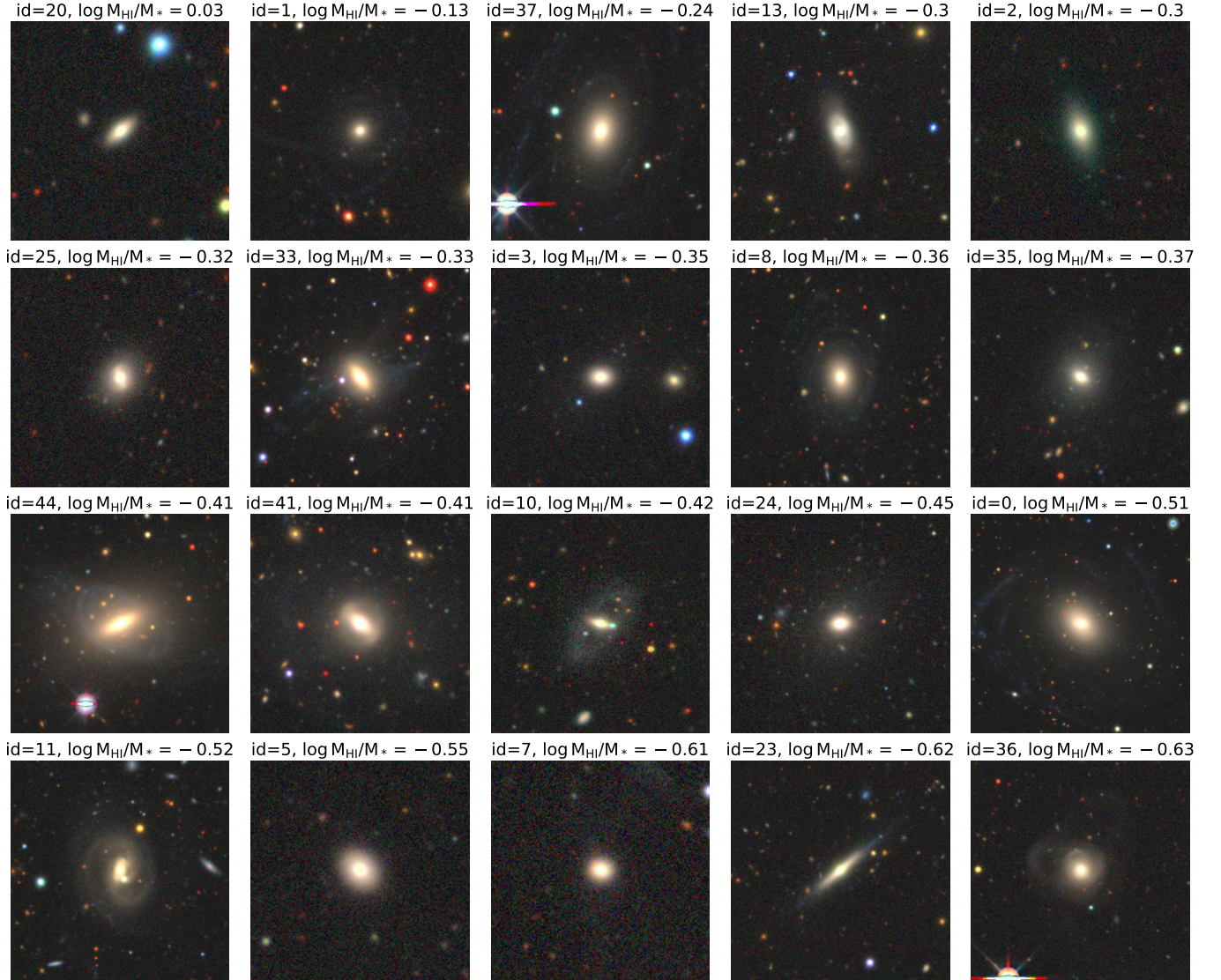


Figure 12. The optical images of the RR galaxies. The galaxies are ordered by decreasing HI-to-stellar mass ratio ($\log_{10} M_{\text{HI}}/M_*$). The galaxy ID from Table 1 and the value of $\log_{10} M_{\text{HI}}/M_*$ for each galaxy are indicated on top of the corresponding image.

⁴ <https://skyserver.sdss.org/dr16/en/home.aspx>

⁵ <https://www.legacysurvey.org>

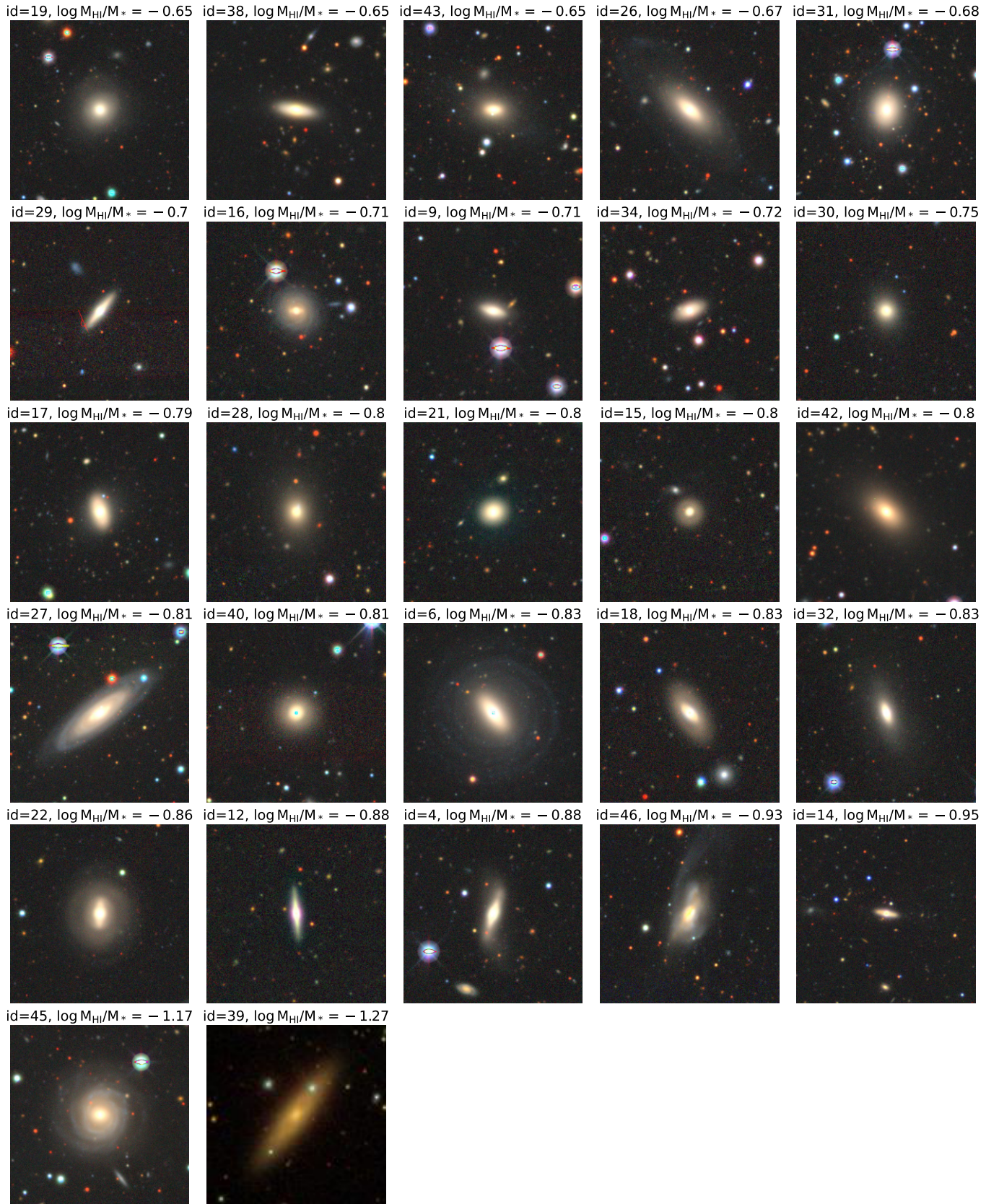


Figure 12. Continued.